Air Force Institute of Technology
AFIT Scholar

Theses and Dissertations | Student Graduate Works

3-2022

Effects of a Nitrogen and Hydrogen Build Atmosphere on the Properties of Additively Manufactured Tungsten

Dana C. Madsen

Follow this and additional works at: https://scholar.afit.edu/etd

 Part of the Manufacturing Commons, and the Structures and Materials Commons

Recommended Citation

Madsen, Dana C., "Effects of a Nitrogen and Hydrogen Build Atmosphere on the Properties of Additively Manufactured Tungsten" (2022). *Theses and Dissertations*. 5440.
https://scholar.afit.edu/etd/5440

This Thesis is brought to you for free and open access by the Student Graduate Works at AFIT Scholar. It has been accepted for inclusion in Theses and Dissertations by an authorized administrator of AFIT Scholar. For more information, please contact AFIT.ENWL.Repository@us.af.mil.

EFFECTS OF A NITROGEN AND HYDROGEN BUILD ATMOSPHERE ON THE PROPERTIES OF ADDITIVELY MANUFACTURED TUNGSTEN

THESIS

Dana C. Madsen, Captain, USAF

AFIT-ENY-MS-22-M-306

DEPARTMENT OF THE AIR FORCE
AIR UNIVERSITY

AIR FORCE INSTITUTE OF TECHNOLOGY

Wright-Patterson Air Force Base, Ohio

DISTRIBUTION STATEMENT A.
APPROVED FOR PUBLIC RELEASE; DISTRIBUTION UNLIMITED.

The views expressed in this thesis are those of the author and do not reflect the official policy or position of the United States Air Force, Department of Defense, or the United States Government. This material is declared a work of the U.S. Government and is not subject to copyright protection in the United States.

AFIT-ENY-MS-22-M-306

EFFECTS OF A NITROGEN AND HYDROGEN BUILD ATMOSPHERE ON THE PROPERTIES OF ADDITIVELY MANUFACTURED TUNGSTEN

THESIS

Presented to the Faculty

Department of Aeronautics and Astronautics

Graduate School of Engineering and Management

Air Force Institute of Technology

Air University

Air Education and Training Command

In Partial Fulfillment of the Requirements for the

Degree of Master of Science in Aeronautical Engineering

Dana C. Madsen, BSME

Captain, USAF

March 2022

DISTRIBUTION STATEMENT A.
APPROVED FOR PUBLIC RELEASE; DISTRIBUTION UNLIMITED.

AFIT-ENY-MS-22-M-306

EFFECTS OF A NITROGEN AND HYDROGEN BUILD ATMOSPHERE ON THE PROPERTIES OF ADDITIVELY MANUFACTURED TUNGSTEN

Dana C. Madsen, BSME

Captain, USAF

Committee Membership:

Chair

Maj. J. S. Brewer, PhD
Member

Dr. C. R. Hartsfield
Member

AFIT-ENY-MS-15-M-000

Abstract

Additively manufactured tungsten was printed in pure nitrogen, nitrogen-2.5% hydrogen, and nitrogen-5% hydrogen atmospheres as part of a 2^3 full factorial designed experiment and subjected to room-temperature and high-temperature three-point-bend testing, chemical analysis, hardness testing, and microstructural imaging techniques. The pure nitrogen specimens exhibited the highest strength and ductility at both high temperature and room temperature. Chemical analysis showed a 2-8x reduction in compositional oxygen relative to unprocessed powder. Hardness values for all samples was between 306.8 and 361.5 HV1. It is proposed that adding hydrogen into the build atmosphere reduced the available energy density for tungsten melting by introducing another competing reaction to that of nitrogen and oxygen, resulting in large cracks and pores in the material. These interruptions in the microstructure resulted in weaker, more brittle metal than that built in a pure nitrogen environment, but the results from the nitrogen environment were comparable in strength range to hot-rolled tungsten.

Acknowledgments

The author would like to acknowledge the entirety of the AFIT AMU team for their invaluable support and assistance in the pursuit of this research, most particularly that of Ms. Brianna Sexton, Ms. Cara Eckley, and Mr. Ryan Kinkade. She further wishes to thank her advisor, Major Ryan Kemnitz, for his excellent guidance, extensive knowledge, and field expertise, all of which were major contributors to the success of these experiments.

Dana C. Madsen

Table of Contents

Page

List of Figures

Page

List of Tables

Page

TITLE

I. Introduction

General Issue

As modern weapons and weapons system evolve, there remains a persistent need for high-strength, high-temperature, oxidation-resistant metals and metal alloys capable of being manufactured into ever more complex geometries. In the past, many of the most desirable shapes have been unachievable by traditional manufacturing methods such as forging, casting, or CNC due to both fineness of required manufacturing tolerances and presence of complex internal voids or ducts in the design for part cooling or other applications during operation. [1]

These are particularly desired for applications in jet engine internal components and hypersonic aircraft, both of which are highly chemically reactive and extremely high-temperature environments. The current material options are limited primarily to highly specialized materials with ablative coatings, both of which must be specially manufactured and are impractical for multi-use vehicles or ceramics, which lack the resilience and toughness of metals and fail both catastrophically and without warning due to their brittleness.

Problem Statement

The Air Force Institute of Technology Additive Manufacturing Unit (AMU) is currently researching possible metals and alloy combinations amenable to additive

manufacturing to find candidates to meet this need. One of the materials under consideration is tungsten, W, due to its high strength and temperature resistance. However, the very attributes which make it desirable for the prospective applications also cause this material to be uniquely challenging to additively manufacture. Most previous attempts have resulted in W which is far weaker and more oxidized than that manufactured using more traditional methods.[2]

However, these problems are unique neither to W nor to the additive manufacturing process. Using additive manufacturing processes on metals frequently has an impact on the resulting material's strength characteristics, and W is notoriously difficult to manufacture. Furthermore, there exist metallurgical techniques that are known to enhance the strength and chemical stability of metals that have yet to be studied in application to additively manufactured W.

Research Objectives/Questions/Hypotheses

Therefore, the purpose of this research was to study the effects of applying one of these techniques to additively manufactured W with the goal of maximizing strength.

Research Focus

The focus of this study was on the effects of build atmosphere composition on W samples.

Investigative Questions

- How can variation of laser scan speed and build atmosphere be used to optimize tungsten material characteristics for use in high-temperature environments?
- What are the material characteristics of tungsten printed in an $N_2 - H_2$ atmosphere?

Methodology

The test articles were subjected to three-point-bend testing at room temperature and at 600°C, chemical composition analysis, Scanning Electron Microscopy (SEM), optical microscopy, and Vickers hardness testing. The results were compared to that of previous research efforts as well as to known properties of traditionally manufactured W.

Assumptions/Limitations

The only process variables that were considered were laser scan speed and atmosphere. There are many other factors that can influence the output of the additive manufacturing process. Also, statistical confidence was not reported for the majority of previous research, which limits the accuracy of comparisons between the data published here and that from other studies.

Implications

This research will aid in characterization of materials resulting from the subject process parameters and establish a basis for further design envelope exploration.

Preview

The background details on tungsten manufacturing, additive manufacturing, and previous research are in Chapter 2. Chapter 3 outlines the experimental design, selection of variables, and the setup for each type of testing and analysis conducted. Chapter 4 covers the results of these test, including both Analysis of Variance (ANOVA) of the designed experiment and qualitative observations, and Chapter 5 provides concluding thoughts and recommendations for future research efforts.

II. Literature Review

Chapter Overview

In this chapter, the background research conducted on the selected metal, tungsten, and previous traditional and additive manufacturing processes used on it.

Tungsten

Tungsten (W) is the 74th element on the periodic table and is part of a group known as refractory metals. Other metals which fall under this classification and are frequently used in manufacturing include molybdenum, tantalum, niobium, and rhenium [3]. As a category, refractory metals tend to have high melting temperatures, high strength, and corrosion resistance, and W is no exception. It has a melting temperature of approximately 3422 ℃ [4] and a documented maximum tensile strength of roughly 980 MPa [5]. Its modulus of elasticity is 390-410 GPa, and hardness value typically ranges from 300-650 HV30 [4]. Unalloyed, it is a relatively brittle metal, and it is prone to oxidation, often forming WO_3, WO_2, and other oxides during processing. These oxides

are considered to be significant weakeners of worked W, and a wide variety of techniques are currently being researched to reduce their formation and effects [6,7].

Pure W can form in three different crystal structures [4]. The rarest and least stable of these is γ-W, a transitional face-centered cubic state which is typically only observed in sputtered W. β-W is also a transitional state and is formed in proximity to W oxides in a Frank-Kasper sigma crystal structure [8]. These two forms are both known to be extremely brittle and will transform to the third and most common structure, α-W, which is a body centered cubic crystal, if enough energy is provided.

Traditional Processing

One of the traditionally manufactured forms of W that has been compared to additively manufacture W due to its anisotropic microstructure is hot-rolled rods. This process begins with the primary working of a sintered ingot at $1500℃ - 1700℃$ [4] to break down the microstructure and reduce the number of pores as well as begin the shaping process.

Multiple reheating and rolling stages are then required to attain the desired rod shape and size since W's high thermal conductivity causes rapid loss of ductility due to cooling, which is counterproductive when attempting to shape metal. The resulting product has a reported strength of 400-800 MPa, depending on its purity and its exact processing conditions [4].

Additive Manufacturing

Additive manufacturing is the process of incrementally constructing an object from some physical medium. This can be achieved in a variety of ways depending on the

material under consideration, but it most frequently involves melting or liquifying a small amount of that material and allowing it to bond to an existing structure as it cools. In this way, objects can be fabricated in a matter of hours with minimal waste and required equipment when compared to traditional manufacturing methods such as casting, milling, or Computer Numerical Control (CNC) machining. Additively manufactured objects can also have extremely complex geometry that would be difficult or even impossible to achieve using alternative methods.

Depending on its application, the resulting article can be used as-is or subjected to post-processing in order to refine it in some way before it is put into service. Additively manufactured articles tend to have rougher finishes and more material discontinuities such as voids, cracks, and foreign particles, so they often require further processing to amend these issues.

One frequently-used post-processing technique used on additively manufactured metals is heat treatment [4]. This process injects heat energy into the object, resulting in increased molecular motion within it. This motion tends to cause the metal molecules and secondary particles within the object to shift into more uniform crystallographic structures that may have been prevented from forming during the build process. Since lack of uniformity can cause unwanted stress concentrations, heat treatment can be used to alleviate some of the problems caused by these stress concentrations such as cracks or voids [4].

General Process

In the case of metal additive manufacturing, one of the most common methods is selective laser sintering (SLS), also known as selective laser melting

(SLM) [9]. This process is conducted within a sealed chamber within a programmable additive manufacturing machine wherein the desired article is built on a movable stage. This stage is first lowered a set distance from the plane in which it is inset and then entirely coated in a fine layer of metal powder, which is brushed over with an arm referred to as a wiper. This metal powder is the medium from which the object will be made. A point laser with enough power to melt the metal is then selectively passed over the stage, only targeting the portions of the powder that are needed to build the first layer or slice of the object. Once the laser has completed its run, the stage is lowered another increment, and the wiper is passed back over it to allow the powder for the next slice of the object to enter the stage. This process is continued until the entire object is built. The excess loose powder is then removed and recycled, and the object is removed from the stage.

Laser Power Effects

One of the determining factors in the success of the build is the laser power. Since the metal is being melted using the energy in the laser, the laser power used must be enough to fully melt the metal. If the laser power is too low, the energy provided may be insufficient to melt all of the powder present in the laser's path, which will cause voids and patches of unmelted powder to be incorporated into the part. However, using too much energy may cause the metal to melt too quickly, resulting in excessive oxidation, burning, and spattering, as well as other modes of energy dissipation, all of which result in flawed and poor-quality builds.

Laser Speed Effects

The amount of time the laser spends in any given area, or dwell time, is also a factor in resulting build quality. While the laser power determines the maximum instantaneous energy that can be introduced to the print medium, the dwell time determines the total amount of energy that portion of the build will need to absorb and how much time in which it will have access to that energy. The effects of heat energy on metal are well-documented and include determination of grain size, amount of cracking, and formation and type of oxides/other secondary particles likely to be present in the resulting metal [1]. Thus, a relatively slow laser speed will typically result in relatively large, columnar grains in the build direction of the part, which often results in anisotropic strength properties in that direction. On the other hand, relatively fast speeds tend to result in nonuniform powder melting and excessive cracking along the laser track since the total amount of energy provided begins to approach the minimum amount required to melt the powder. This could cause insufficient melting, which would then be followed by rapid cooling and contraction of the melted portions. As a result, the recently melted section tends to incompletely adhere to the surrounding portions of the part [6].

Atmospheric Effects

The atmosphere in which the object is build will also have an effect on its quality. For instance, while some metals do not oxidize at room temperature, the majority do when approaching their melting temperature. Since the additive manufacturing process heats the metal up to its melting point, the metal reaches

its oxidation temperature range both as it is being heated and as it cools down after the laser has passed by. During these periods, there is a chance that the metal will react with the O_2 present in the build chamber atmosphere if any is present. Since oxidation tends to negatively affect the strength and ductility of most metals, experiments have been conducted regarding the effects of sealing the build chamber and pumping it with an alternative atmosphere which does not include O_2, such as Ar or other noble gases [7]. Other alternative atmospheres will include a gas which has a lower activation energy for its reaction with O_2 such as N_2 or H_2, such that the O_2 will preferentially form bonds with that gas rather than bonding with the metal to form oxides [10].

There are drawbacks to using exotic atmospheres, however. First, it increases the processing cost for the build in the form of equipment costs and the costs of procuring and installing the gases. Secondly, the build chambers are difficult to entirely seal, which can result in either unwanted O_2 leaking in or hazardous gases leaking out. Some of the alternative atmospheres are heavier than air, which could cause an unsafe buildup of such gases to settle on the manufacturing floor and deprive the occupants of air if not carefully monitored.

N_2

Nitrogen composes roughly 80% of standard atmospheric air and is therefore present in the majority of metal additive manufacturing builds. However, the purpose of changing the atmosphere to entirely N_2 when printing W is twofold. Firstly, N_2 does not readily react with W [4], so it is unlikely to form unwanted secondary phase particles within the metal.

Secondly, N_2 does react with O_2 at high temperatures to form NO, N_2O, and NO_2 and the activation energy required for these reactions is lower than that required to form WO_3. [11,12] Since the energy required to cause any one of the $N_2 + O_2$ reactions is lower, they would theoretically consume all of the available O_2 present in the build chamber and prevent the formation of WO_3 as a result.

H_2

Hydrogen is also present in trace amounts in atmospheric air, mainly in the form of water vapor. The goal of adding H_2 to the build chamber atmosphere when printing W is to reduce oxidation by causing the O_2 to bond with the H_2, forming water or water vapor instead [7]. The H_2+O_2 reaction has an activation energy which is lower than that of W and O_2 [12,13], and the resulting product of H_2O is also less potentially harmful to humans than NO, N_2O, or NO_2. H_2 is also unreactive with W [4], which theoretically reduces the possible sources for secondary phase particles.

Layer Thickness Effects

The thickness of each layer or slice of the build will determine the amount of powder the laser will be required to melt at any given point along its track. If the layer is too thin, it may be difficult to appropriately scale the power of the laser down to the volume of the powder such that optimum melting is achieved. On the other hand, if the layer is too thick, the energy may not penetrate entirely

through the powder layer or be sufficient to fully melt the entire volume, resulting in poor layer adhesion [9].

Layer Orientation Effects

The laser's path over the powder can be varied on each layer if desired, since it is controlled by a computer program. Since one of the drawbacks of additive manufacturing is the anisotropic properties of the resulting material (e.g., long, columnar grains in the build direction or poor adhesion between layers resulting in long fibers of metal in the direction of the laser's path), it has been posited that randomizing or at least alternating the laser path orientation between layers could result in greater isotropy, much like is frequently done in composite manufacturing [9]. While research is being done in this area that is promising, there are some qualities unique to additive manufacturing that inhibit this goal.

Unlike in composites, the only adhesive agent in additive manufacturing is the bonding of the melted material to the existing structure. Furthermore, the resulting local structure formed in terms of grain size, secondary particles/impurities, and success of adhesion is a function of the amount of heat energy present in that portion of the material. As a result, shifting or randomizing the layer orientation, which can result in uneven material cooling, can result in nonisotropic or discontinuous material properties [9]. Such characteristics are typically associated with weaker and more brittle resulting metals and are therefore disadvantageous. Therefore, randomized and shifted layer orientations are less common, since the most effective method of ensuring uniform temperature distribution is to repeat the same path over every layer. In the cases

where layer orientation is varied, care must be taken to ensuring that the pattern does not result in uneven cooling.

Previous Research

The strongest influence on the experiment analyzed in this paper was the previous research conducted by the AFIT AMU on alternative build atmospheres. Their most recent study in this vein is one on the benefits of an Ar versus $\mathrm{Ar} - 3\%\mathrm{H}_2$ atmosphere, [7] and the results of this research were of particular interest, since one of the variables of greatest interest in the current experimentation is the percentage of H_2 in the build chamber. This experiment was conducted using pure W powder to produce 2 mm x 4 mm x 18 mm test specimens in both build environments for comparison.

According to their report, they found that the amount of oxygen present in the samples they built in the $3\%\mathrm{H}_2$ atmosphere was three to five times greater than that of the raw powder, while those built in pure Ar exhibited a slight reduction in oxygen content. Since there was no purposeful addition of oxygen to the build chamber in either atmosphere, the additional oxygen was conjectured to have been introduced to the part due to water deposits on the surface of the part as it was being built. This water would have been created from the H_2 introduced to the build atmosphere combining with the O_2 infiltrating the build chamber from the outside air. The activation energy for these two components to create $\mathrm{H}_2\mathrm{O}$ would have been reached near the laser and the surface of the current layer of the part during the build, but the bonds would then have been quickly dissociated upon the water depositing itself on the molten W surface. The oxygen would then have been drawn into an oxidation reaction with the W, resulting in more constituent

oxygen in these parts than those built in the pure Ar atmosphere. It was further conjectured that the H_2 was consuming the necessary energy for WO_3 sublimation, so instead, further energy inputs were resulting in H_2O and WO_2, instead.

They also found that the $3\%H_2$ samples also had significantly smaller grain sizes, and it was thus hypothesized that this was due to the presence of the WO_2 preventing grain growth. However, it was noted that WO_2 is stronger and more stable than WO_3, so these smaller grains with theoretically stronger grain boundaries were likely to result in stronger test specimens.

The AMU researchers then tested their hypotheses regarding the sample strengths via three-point-bend testing and found that the samples processed in $3\%H_2$ were indeed stronger. Their best-performing specimen had a strength of 985 MPa, which they found competitive with W processed by more traditional methods.

Since it would build directly upon their previous work, the present research on an $N_2 - H_2$ build atmosphere was anticipated to produce similar trends. However, some differences were expected due to the complications that could arise from the possible competing reactions between N_2 and H_2.

Other previous AMU research also provided guidance in scoping this experiment, including a study on the combined effects of refractory alloys and post-processing heat treatments [6]. The resulting paper compared pure W, W-5%Re, and W-25%Re subjected to two different types and lengths of heat treatment. It also provided more data on previous strength tests, which were of interest since strength testing was a major component of the present experimentation.

The relative grain sizes and types of the pure W and alloys was also reported. The pure W had large, long columnar grains in the build direction, but the introduction of increasing amounts of Re appeared to break up these large grains. It was reasoned that the increase in grain boundary surface area should positively affect strength and material density by reducing O impurity concentration at these boundaries. The heat treatments also had a measurable effect on the grains, predictably increasing their size and decreasing their directionality.

The strength of W processed in Ar subjected to uniaxial tensile testing was unobtainable since all tested samples broke immediately upon load application [6]. However, values of up to 659.8 MPa were reported from the W-25%Re, providing a target to match in the present experimentation, which will use alternate methods of O_2 reduction in the samples. Since the heat treatments in this study took up to 12 hours to conduct, if similar results could be achieved by altering the build atmosphere instead, that could result in shorter part lead times.

Since an objective of this research was to prevent the formation of and reduce the amount of secondary-phase particles in the finished material, it was beneficial to investigate what formations of these particles might look like under the SEM. One source of information written by Venables and Brown addressed what types of formations WO_3 and WO_2 tended to present at high temperatures in the presence of H_2 [14]. The researchers noted thin crystalline structures formed within the first minute or so, after which more amorphous structures reminiscent of coral began to proliferate. Since high-temperature testing was part of the test campaign, it was reasonable to expect that similar

structures would be found on the high-temperature testing samples. If encountered, these formations would now be able to be appropriately identified.

Another major detractor from the strength of additively manufactured W is the high percentage of cracking and voids present in the resulting metal. A paper that discussed its microstructure in detail was “Pure Tungsten and Oxide Dispersion Strengthened Tungsten Manufactured by Selective Laser Melting: Microstructure and Crack Mechanism” by Hu, et al. In their work, they discussed some of the reasons that W is so prone to cracking during the additive manufacturing process [1].

The first culprit mentioned is the high surface tension of molten W. Strong covalent bonds within the metal prevent the metal from spreading out and pooling to the extent that metals with lower melting temperatures would. As a result, the molten W adheres more closely to itself than it does to the existing structure outside of its molten surface, and it splits away from its surroundings as it cools and shrinks.

The other mechanism discussed is the introduction of impurities into the pure W during manufacturing. These impurities tend to be pushed to the grain boundaries, resulting in weaker grain boundary strength. Later on in their paper, they detail the effects of these impurities, particularly WO_3 and WO_2. When aggregated at the grain boundaries, these oxides prevent grain dislocation motion, causing stress to build up locally and cause transgranular fracture instead of plastically deforming. They also examined the effects of the oxides at during cooling, noting that the different cooling rates of the oxides and the pure W cause cracks to form at the grain boundaries.

While the method of overcoming these issues in the study was the introduction of secondary-phase particles, altering the build atmosphere to something other than air

should address the level of impurities in the W by both consuming any interloping O_2 in atmospheric reactions and by reducing the amount of O_2 present to begin with. By the logic presented in their research, this should result in a denser and stronger metal.

Since cracking is known to undermine the strength properties of W, studies were sought regarding the mechanisms which promote cracking. One such paper by Vrancken, et al, specified ductile-to-brittle transition temperature (DBTT) and the size of the power-to-speed (P/v) ratio as the driving factors in the severity of cracking in additively manufactured W [15]. It was shown that the amount of cracking has an inverse relationship with the P/v ratio. In the present experiment, the power was held constant at 200 W, so the amount of cracking was expected to increase with print speed.

Other recent work in W additive manufacturing includes a paper by Iveković et al [16], which delved into variations in the SLM process and some of their effects on density, microstructure, and cracking of the finished products. The main foci of this research were the effects of preheating the build plate above the DBTT for W and alloying the W powder with another refractory metal, Ta. They also varied energy density, a function of layer orientation, scan speed, laser power, layer thickness, and hatch spacing. The energy density range tested was from approximately 100-1000 J/mm^3, and the results for pure W showed an increase in density from approximately 80% at 100 J/mm^3 to 92-97% at 200-400 J/mm^3, depending on the printer. After that point, there appeared to be minimal change in density.

No analysis was included regarding the impact each variable within the energy density figure had, but it did in general indicate that increasing power and decreasing

scan speed, layer thickness, or hatch spacing would result in a denser final product within the tested range.

Comparisons between the microstructure of W and W-5%Ta and of that resulting from heated and unheated build plates were also discussed. The introduction of Ta was found to reduce but not eliminate cracking and therefore increase density. However, heating the build plate did not appear to significantly alter the amount or type of cracking present. The authors speculated that this was likely due to the presence of atmospheric O_2 in the build chamber causing oxidation and shifting the DBTT higher than the preheating temperature they selected.

The results of this study directly impacted the variable selection for this experiment by highlighting the importance of controlling the build atmosphere for room-temperature SLM. This, along with the results of the $Ar - H_2$ study,[7] narrowed the present experiment's focus to the effects of an $N_2 - H_2$ processing atmosphere. It also confirmed that given a set laser power, variation of scan speed should have a significant effect on material density, and by extension, material strength.

Since it has proven uniquely challenging to avoid impurities within additively manufactured W, research results were also sought on the effects of secondary particles on W material properties. One such study by Gludovatz, et al, focused on impact to W fracture mechanics [17]. The fracture surfaces of ten samples with varying impurity levels and microstructures were examined via SEM and Auger electron spectroscopy, and it was found that grain boundary impurities were not a driving factor in fracture resistance. Instead, microstructure type and deformation which led to intragranular dislocations were determined to be of greater relevance. This finding is of particular

importance to the study of additively manufactured W because misalignments within its grains and grain structures are common, [4] and their presence could be a factor in weakening it.

Much consideration was given to selecting which would be the most profitable factors to vary in the experiment that was designed for this study. Such decisions are informed, when possible, by factors that have proven significant in previous designed experiments with similar subjects. While few examples were available for SLS on any form of W, one of the few available was a study by Ghosh, et al,[2] who used the Taguchi method to study the SLS process of a tungsten carbide (WC) and cobalt (Co) alloy.

The Taguchi method is a of experimental design based on the methods pioneered by R. A. Fisher, but their interpretation and implementation is more sophisticated than a simple full factorial design [18]. However, the processes of factor selection and identification of significant factors is the same for both variations of these statistical methods, so the results of their study still have bearing on the current experiment. The original factors they selected included the percentage of Co versus WC, layer thickness, laser power, powder composition, hatch spacing, pulse width, and focal plane distance. The responses they chose to consider included porosity, density, and microhardness.

After testing, the researchers performed an ANOVA and optimization based on their goals for each response, and in the case of this alloy, it was found that hatch spacing and alloy composition were the two determining factors in achieving the optimal results of maximizing density and hardness while minimizing porosity. Although the importance of these factors on the current experimentation was considered, it was determined that

alloy composition was out of scope (although a potential candidate for future research), and hatch spacing had proved to have little effect on previous additive manufacturing efforts in the AFIT AMU. Therefore, more promising factors were ultimately selected for the design.

The factor with the least previous research available was the atmospheric effects of N_2 and H_2. One of the few studies which has been done regarding the effects of a pure N_2 environment on additively manufactured W was a comparison between W printed in an N_2 atmosphere versus that printed in an Ar atmosphere [10]. In this study, 99.9% pure W powder was used to print specimens at a range of 400-600 mm/s and 400W and 450W power. The samples were then imaged and tested.

It was found that the samples printed in N_2 were smoother and less porous, resulting in denser material. However, both sets of samples exhibited roughly the same amount of cracking, and their general microstructure appeared similar.

Despite these similarities, it was shown that the pure N_2 specimens had a higher Vickers hardness (410-460) and maximum compressive and bending strength values (1074 MPa and 153 MPa, respectively) than Ar. The findings in their paper informed expectations regarding the present experimentation as well as confirming that an N_2 atmosphere had a reasonable likelihood of producing specimens with superior material properties to those formed in pure Ar in previous studies.

The addition of atmospheric H_2 into the build chamber is a major component of the current body of experiments, but the use of H_2 in the reduction and purification of W and W powders is not a new science. Many of the same chemical interactions and results were likely to contribute to the behavior of the additively manufactured material made

during the course of these experiments, so previously publications on W production techniques using H_2 were consulted.

In a series of papers written by Schubert and Lassner in 1991, the details of oxide reduction using H_2 at 600-700℃ were discussed [19]. Under dry conditions, the H_2 reacts with the oxygen present in WO_3 in a progressive chain:

$$WO_3 \rightarrow WO_{2.9} \rightarrow \beta - W \rightarrow \alpha - W \quad (1)$$

The entire sequence of reactions will occur, provided there is sufficient H_2. However, if insufficient H_2 is present, there may be residual oxides in various configurations still remaining in the finished piece. Since the percentage of H_2 that was added to the build atmosphere was relatively low, it was likely that any WO_3 formed would not be able to completely react with the H_2 in the build chamber. This indicated that the oxides listed in the above reaction could be found in various quantities throughout the samples.

A notable aside from the main discourse in their paper is the discussion of the wide variant of colors the oxides are known to exhibit based on the circumstance under which they were formed. These are known to vary in color spectrum from yellow to violet and may be able to be used as a visual indication of these oxides during the current experiments.

Another factor of interest was the behavior of printed W at high temperatures -up to 600℃ within the scope of this experiment. A paper published by Vesel, et al, addressed the behavior of oxide films formed in a temperature range from 600℃ − 1100℃ [20]. In their background research, they noted that the oxides previously observed in this temperature range began with the formation of a layer of $W_{18}O_{49}$, which then cracked under prolonged exposure to heat and formed $WO_{2.92}$ followed by WO_3 as

the temperature was continually increased. They also noted that at higher temperatures, the resulting WO_3 has been shown to rapidly react and expose the underlying W to the atmosphere, and causing a cycle of oxidation and sublimation. This caused the exposed W to be consumed in the course of the reaction and led the researchers to suggest chromium oxide film barriers as a possible deterrent to this degradation.

During the course of their own experimentation, they confirmed the formation of the three oxides in the previously stated order, noting that they were formed after even very short terms of exposure. Although the present experimental campaign is only planned to reach the lower bounds of the temperature range that these researchers explored, their work would indicate the possibility that $W_{18}O_{49}$, $WO_{2.92}$, and WO_3 may be present on the surfaces of the high-temperature test samples.

Previous research on the effects of temperature on W was also found in a paper by Rupp and Weygand [20]. The effects of a wide temperature range (-150℃ to 950℃) on the fracture toughness of rolled W rods was been investigated, and particular note was taken in the change from brittle to ductile fracture modes as the metal reached its DBTT. In this study, samples from the rods were cut for single edge notched bend (SENB) testing and notched parallel and perpendicular to the rolling direction to determine any differences in fracture toughness based on crack orientation relative to the characteristically long, columnar grains formed parallel to the rolling direction. The study found that the specimens notched perpendicular to the rolling direction were significantly tougher than those notched parallel, confirming that the anisotropy in the rolling direction was indeed a determining factor in the crack resistance of the material.

It was also observed that the fracture mode and fracture toughness was affected as the test temperature was varied. Regardless of crack orientation, the fracture toughnesses of the samples were lowest at $-150℃$ and reached their peaks between $500℃$-$600℃$ before tapering off with further temperature increases. The fracture modes were also noted to have changed from pure brittle inter- and trans-granular fracture to some inclusions of plastic deformation as the test temperature moved into and beyond the DBTT.

One of the chosen factors under consideration was the laser scan speed, and study results were sought to establish what type of trends to expect in the present experimental data based on past research. One such study by Simchi [9], although conducted on iron alloys instead of W, found that there was a semi-logarithmic relationship between increased fractional density, which is typically considered a positive indication of superior strength,[4] and decreased laser speed. However, it was noted that other studies had discovered a limit to these benefits. At higher laser powers, lower scan rates led to delamination and cracking between build layers. Since different metals absorb heat at different rates and disperse energy within themselves differently, it is likely that there will be differences between two different metals' reactions to a given laser power and scan rate. However, it is reasonable to suppose that there would be enough similarities between them that they would have the same general trends of delamination at higher power and decreased density with increased scan rate.

Summary

W is an extremely strong and temperature-resistant refractory metal with attributes highly desirable for high-temperature applications. Since those applications require complex geometry only achievable via additive manufacturing processes, optimized SLM processes are being researched. Promising material properties have been achieved by changing the build chamber atmosphere, but very little research has been published in this area regarding an $N_2 - H_2$ atmosphere. Previous research on W material properties and additive manufacturing processes was sought to inform the scope and expected results of the current experiment.

III. Methodology

Chapter Overview

This chapter will describe the methodology used to conduct testing.

Design of Experiments

Theory

Design of Experiments as a method was pioneered in the 1920s-30s by R. A. Fisher, a statistician hired to determine the best conditions under which to cultivate certain crops [22]. During the course of his work, he found that serial single-variable experimentation was impractical when attempting to statistically model and predict outcomes that depended on multiple variables. Copious amounts of lengthy tests were necessary to achieve the randomization necessary to ensure that a normal distribution representative of the global outcome was presented in his data. Given the length of time over which each data point was

collected, it was difficult to account for the effects of the variables which were not being directly controlled over the course of a given single-variable experiments, and as a result, large bodies of data collected over many years were unusable.

For instance, if the efficacy of a fertilizer were being tested, a randomized single-variable experiment could consist of a certain number of plots of land contained within a field which would either be fertilized or unfertilized. Over the course of a growing season, data on the height or production (or some other desirable metric) would be collected, and a line model would be generated to best fit the data. However, there are a variety of factors besides the presence or absence of fertilizer that could have affected the results, such as time of year, soil moisture, amount of shade, amount of pests present in each plot, consistency and type of soil, or any number of other complicating variables. All of these factors would be lumped into the model error or the data noise floor and therefore preventing a statistically sound model from being derived. These unaccounted-for factors could just as easily be argued to have caused any apparent trends in the data as could the introduction of the fertilizer, rendering the entire body of data unusable.

He therefore developed a discipline of multivariable experimentation, which he dubbed, “Design of Experiments” in his 1935 book of the same title, that could statistically account for the contributions from multiple variables to an outcome within a single experiment [23]. This lowers the amount of residual random error and lowers the noise floor for the experiment, allowing much higher confidence in the accuracy of the models derived from its data.

He further found that the trends present in the entire body of data could be represented with high accuracy using only the extreme ends of each variable's range, vastly decreasing the number of test articles or cases required from thousands to 2^x, where x is equal to the number of variables or factors. The range of the variables under consideration can also be extended further with the addition of only two or three points per factor, making this method ideal for exploratory research.

If the system response is expected to be nonlinear, a curvature check can be conducted by conducting two to three tests at the centerpoint of all factors' ranges. If the response is linear, this curvature check can be eliminated from the model with no impact on model accuracy. If the response does show curvature, the model will be able to better fit the data, improving the optimization capability of the model.

The design of experiments process is agnostic to any system with continuously varying factors and can even be modified to account for discrete variance, although this results in lower statistical confidence. This is particularly helpful in the case of apparatus-based testing, since the goal of a designed experiment is to provide a high degree of repeatability regardless of the equipment used. The variance innate to any unique system is ascribed to the error or noise floor in the model, so assuming appropriate calibration, the system behavior will match the trends in the statistical model regardless of the make and model of the equipment.

Statistical confidence is a measure of how likely it is that the data collected during the course of an experiment is an accurate reflection of the global data [23]. The higher the statistical confidence of an experiment, the lower the likelihood that any trends present in the data are the result of anything other than the variables included within the scope of the experiment.

Using the Design of Experiments method for W additive manufacturing research will build a statistically supported base from which to establish trends in additively manufacture W strength and ductility subjected to the selected processing conditions. Much of the work in this field up to this point has been based on singular or serial demonstrations rather than statistically-driven experimentation methods. This body of work resulted in 99% confidence models that can be practically and reliably applied in commercial manufacturing and easily expanded upon with subsequent designed experimentation in the future.

Experimental Design

One of the experiments of highest interest was a comparison between a selection of different atmospheric conditions during processing. W is prone to oxide formation at high temperatures, and these oxides adversely affect the strength and ductility of the sintered metal. In an effort to reduce oxide formation, two methods are typically employed: purging the build chamber of oxygen through addition of an alternate gas or introducing a gas with which oxygen reacts with more readily than it does with W. The design selected for this experiment

was 3-factor full factorial with three replications and three centerpoints, resulting in a 99.7% confidence model, shown in Table 1.

Table 1. Experiment Design for Variable Atmosphere

Run	Speed (mm/s)	Test Temperature (℃)	$\%H_2$	Run	Speed (mm/s)	Test Temperature (℃)	$\%H_2$
1	600	600	5	15	350	310	2.5
2	100	20	0	16	600	20	5
3	600	600	0	17	100	20	5
4	600	600	0	18	350	310	2.5
5	600	20	5	19	100	600	5
6	350	310	2.5	20	600	600	5
7	100	20	0	21	100	600	5
8	100	600	0	22	600	600	5
9	600	20	5	23	600	600	0
10	100	20	5	24	100	20	0
11	600	20	0	25	100	600	5
12	100	20	5	26	600	20	0
13	100	600	0	27	600	20	0
14	100	600	0				

Factor 1: Bend Test Temperature

600 ℃ is past the DBTT of W [4]. Since the behavior of W is therefore known to change beyond this temperature and the presumed applications of the metals processed will be greater than 600 ℃, it was desirable to observe the effect of increased operational temperatures in general with the understanding that the findings could be generalized to the other cases.

This factor had a range of 20-600 ℃ and was a continuous variable since it could be varied with relatively fine granularity. The range was chosen in order to ensure that it encompassed the entire range of the

DBTT for W, which is 200-400 ℃ [4]. This was intended to ensure exhibition of both brittle and ductile W behavior in the response data.

Factor 2: $\%H_2$

In previous studies,[7] atmospheric H_2 has been shown to positively affect the properties of laser sintered W by reacting with the O_2 present in the processing chamber and therefore reducing the amount of O_2 available for the production of oxides. It was therefore hypothesized that the introduction of H_2 into the N_2 atmosphere could result in a combined further reduction of W oxides present in the final product since both N_2 and H_2 react with O_2. In order to test this hypothesis, a range of 0%-5% H_2 was introduced into the N_2 environment.

Factor 3: Speed

The laser speed or dwell time during the sintering process has also proven to have an effect on the resulting qualities of W in previous studies [6,7,8]. It is widely believed that there are optimized dwell times for any given processing conditions or operational applications, so the primary factor in many studies is laser speed. Previous demonstrations have suggested that for the printer used for this experiment, the optimum speed should lie within the range of 100-600 mm/s [6]. Within this range, it has typically been shown that a speed of 100 mm/s results in the most thorough powder melting since it is the longest dwell time. This allows for the growth of larger grains in the build direction and fewer, smaller pores. At a speed of 600 mm/s, while the grain sizes are typically appreciably

smaller than at slower speeds, there is a significant increase in unmelted powder and pore size that dominates the characteristics of the material.

Test Methodology

A variety of tests and techniques were employed to acquire the response data for each experiment, with the goal of fully characterizing each sample's properties.

Sample Manufacture

Figure 1. GE Additive/Concept Laser MLab 200R Cusing Printer

All samples were built using a Concept Laser MLAB Cusing 200R 3D metal printer (Fig. 1) with a 200 W Yb:YAG continuous-wave fiber laser with a focus diameter of 50 μm and a wavelength of 1080 nm. The powder used was Tekna W-25 [37]. Each layer had a thickness of 20 μm and 50 μm hatch spacing.

Sample Preparation

Figure 2. Buehler Ecomet 300 Grinder and Polisher

The samples used for mechanical testing were polished with 320-grit SiC sandpaper to remove any residual scale from the additive manufacturing process. This was accomplished using the Buehler Ecomet 300 Grinder and Polisher shown in Fig. 2. The specimens were then dried in the OmegaLux LMF 3550 Benchtop Muffler Furnace shown in Fig. 3 for one hour at 120℃.

Figure 3. OmegaLux LMF 3550 Benchtop Muffler Furnace

Three-Point-Bend Test

Three samples of each material with recorded dimensions were subjected to a room-temperature three-point bend test. This test is a measure of a material's tensile strength and ductility conducted by subjecting a nominally 2x4x18 mm sample to a load in the center while resisting support is provided at the sample's ends, as illustrated in Fig. 4.

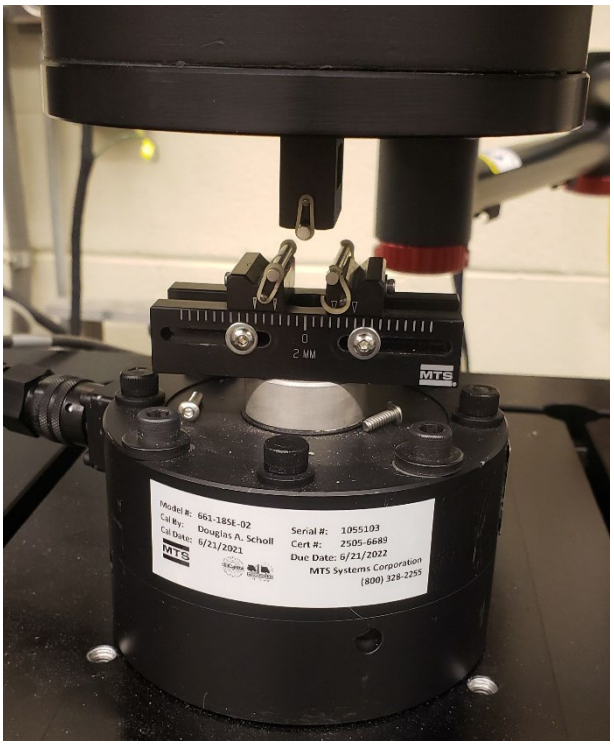

Figure 4. Three-Point-Bend Test Loading Fixture

It is often used in rapid prototyping scenarios because the required specimen size is significantly smaller than that for a uniaxial tensile test [24]. During the test, the load and displacement on the sample is recorded until failure, which allows its maximum and failure strength and ductility to be determined. Since each sample is tested separately and a full reset is conducted between each test, each of the data points collected in this experiment is treated as a unique response independent of previous tests. An MTS Acumen electrodynamic three-point-bend machine was used to conduct the experiment.

The raw data gathered during this testing was processed using the Matlab code provided in Appendix A [25]. This code, written by Major Ryan Kemnitz and Ms. Brianna Sexton, uploads the raw data files into Matlab, locates the

maximum load and displacement data points, and calculates the maximum stress and strain of the sample using those data points. Similarly, the break stress and strain are found by determining the break load and displacement points in the data.

High-Temperature Three-Point-Bend Test

In the first experiment, each W variant was also subjected to a 600 ℃ three-point-bend test to characterize effects of processing atmosphere on the DBTT and general high-temperature characteristics of the metal. The resulting data from this test were the same as for the room temperature three-point bend test, but the setup instead included a Material Test System 653 furnace enclosing the test fixture and a Material Test System 409.83 temperature controller. Also, the test apparatus was a hydraulically powered Material Test System 810 test frame.

The raw data from this test was processed using another Matlab code written by Major Ryan Kemnitz and Ms. Brianna Sexton, and this code is included in Appendix B [26]. Similar to the Matlab code for the room temperature three-point bend test data, it returns the maximum and break stress and strain for each sample's data.

SEM/Microscopic Imagery

Figure 5. Three-Point-Bend Test Loading Fixture

After testing the samples until failure, they were next examined under both an optical and scanning electron microscope (SEM). First, the raw fracture surfaces were examined via a Tescan MAIA3 SEM (shown in Fig 5) to qualitatively determine characteristics such as crack initiation points, build uniformity, level of oxidation present, and types of anomalies.

Figure 6. Metlab MetPress A

A selection of mechanical test samples were mounted lengthwise in carbon pucks subsequent to testing: a representative specimen built in each atmosphere at each print speed was included for a total of twelve samples in three pucks. Each puck contained one set of samples processed under different atmospheric conditions. This was achieved by use of the MetLab MetPress A shown in Fig. 6, and a representative carbon puck is included in Fig. 7. These pucks were then polished with the Buehler Ecomet 300 Grinder and Polisher to reveal the grain structure and pore density of each sample group.

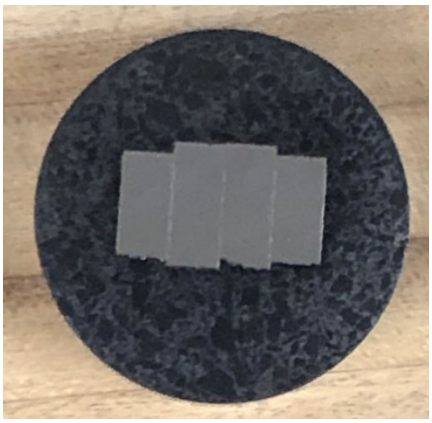

Figure 7. Carbon Puck

The specimens were examined on an Observer.Z1m inverted optical microscope, shown in Fig 8.

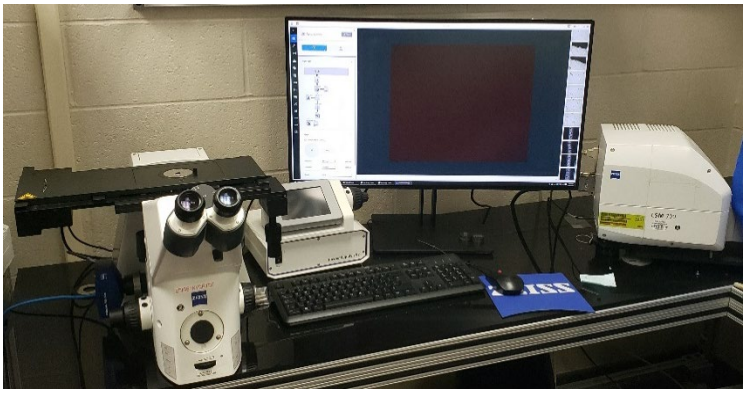

Figure 8. Observer.Z1m Optical Microscope

Pictures of the grains, surface pores, and imperfections were taken and analyzed using Zeiss image analysis software, providing a pore count and individual pore size measurement for each specimen.

Hardness Testing

Figure 9. QATM Qness Hardness Tester

Samples from each processing run were also subjected to Vickers hardness testing on the QATM Qness Vickers Hardness Tester at the Air Force Research Lab (AFRL), a representative image of which is shown in Fig 9. Vickers hardness is a unique characteristic of a material and can be used to determine strength and ductility within a certain range provided there is preexisting data on the material as processed.

While this data is less reliable than conducting an actual tensile test, it is significantly faster and cheaper and is often used in both quality control and unknown material characterization. During a hardness test, a sample of the subject material is first affixed to the test apparatus. Once it is secure, a relatively defect-free section of the material is selected, sometimes with the aid of an optical microscope, and a diamond-tipped tool head of known dimensions in the shape of a 136° pyramid is applied to the surface of the material with a specific amount of force (typically recorded in terms of kgf) for a specific length of time (typically

on the order of 10-15 s). The force and duration of the application are recorded in the resulting hardness value in the format: XXXHVYY/ZZ, where XXX indicates the location of the hardness value number, YY would be the load in kgf, and ZZ would record the time length of the application if it differed from 10-15 s. This process is typically repeated roughly ten times per specimen. The dimensions of the resulting indentations in the surface of each sample are then microscopically measured, which are then used to calculate hardness values via the following equation:

$$HV = \frac{1.854 * F}{d^2} \quad (2)$$

Where:

F = load in kgf
d^2 = area of the imprint from the diamond tip in mm^2 [27]

The individual hardness values collected from a given sample are then averaged, and the resulting number is reported as the hardness value for the sample. Typical hardness values for a given material are reported in ranges since the exact reported value depends heavily on the sample and testing conditions. Defects or cracking within or near the indentation have a large effect on the measurements, as do human or machine measurement error, and small changes in the reported dimensions of the indentation have a large effect on the resulting hardness value. Since there can be a wide variance in the reported hardness value of a material, this is considered a less precise determination of a material's attributes than a three-point bend or traditional tensile test.

All eligible quantitative data was statistically analyzed using Design-Expert 13, an experimental design and statistical analysis software produced by Stat-Ease [28].

Chemical Composition Analysis

It is also useful to determine the resulting chemical makeup of the processed samples to establish any trends in resulting H, N, or O content. The abundance of these elements can help predict expected performance of the resulting material by indicating the amount of secondary particles such as oxides, since these are known to reduce overall material strength. The analysis was conducted by Luvak, Inc, in Boylston, MA, and each set of data points is the averaged results from three samples of the printed material.

Summary

An experimental design based on the statistical methods developed by R. A. Fisher was used to run an experiment streamlined for ANOVA processing on pure W printed in a primarily N_2 atmosphere with 0-5% H_2 at 100 mm/s to 600 mm/s speed and tested at room temperature and 600℃. The fracture surfaces of the samples were then examined via SEM, and the pores and grains were imaged via optical microscopy. The imaged samples were then subjected to Vickers hardness testing. Finally, specimens from each printed batch at each speed were submitted for chemical analysis to determine the amount of N, O, and H present in each.

IV. Analysis and Results

Chapter Overview

The analyses and results section begins first with the purely quantitative data and ANOVAs of the designed experiment response models. Following these, the qualitative analyses from imagery are presented, and finally, the hardness data is discussed.

Chemical Composition Analysis

Table 2. Chemical Composition Results from Pure W samples processed in 100% N_2, 2.5% H_2, and 5% H_2

Atmosphere	Speed (mm/s)	Oxygen (ppm)	Nitrogen (ppm)	Hydrogen (ppm)
N2	100	71	101	6
N2	200	118	101	6
N2	400	125	110	<5
N2	600	139	111	<5
2.5 H2	100	73	86	<5
2.5 H2	200	52	93	<5
2.5 H2	400	165	103	<5
2.5 H2	600	92	109	<5
5 H2	100	31	81	<5
5 H2	200	103	82	<5
5 H2	400	85	93	<5
5 H2	600	100	97	<5
	Unprocessed Powder	259	5	12

The results of the chemical composition testing shown in Table 2 exhibited remarkably low O_2 content in all analyzed samples regardless of atmosphere or processing speed, particularly when compared to results from previous experiments conducted on samples processed in $Ar - H_2$, shown in Table 3. Furthermore, while both raw powder samples were somewhat similar in original composition, the samples from

the $Ar - H_2$ experiment gained a significant amount of O while those from the $N_2 - H_2$ experiment lost O, instead. There also appears to be some indication of opposite trends in O amount between the two studies relative to speed. In the $Ar - H_2$ study, increasing laser speed resulted in lower O concentration in the samples processed in the 3% H_2 environment. However, the results from the $N_2 - H_2$ study show instead that regardless of atmospheric H_2 percentage, increasing laser speed causes slightly higher amounts of O.

The amount of N_2 present in all processed samples in Table 2 is higher than that of the unprocessed powder, and there are conflicting trends between the amount of H_2 in the build chamber and the laser speed relative to this response. As might reasonably be expected, adding H_2 drove the overall amount of N in the final sample composition down. However, the faster the laser speed, the more N entered into the sample. This could indicate that the atmospheric N_2 permeating the powder during the sintering process is reacting with the O_2 using the energy provided by longer laser dwell times, driving the overall amounts of both N and O remaining in the material to go down.

According to research by Dong et al, the amount of nitrogen integrated into the material between the primarily N_2 atmosphere and the primarily Ar atmosphere should be relatively similar, so any differences in material properties is unlikely to be due to the added N alone [10]. The hydrogen content was relatively unchanged regardless of atmosphere or laser speed, indicating that residual hydrogen is not present or a significant factor in resulting properties. The effect of H and N on the content of O may be the most significant effect of these gases.

Table 3. Chemical Composition Analysis from $Ar - H_2$ Processing Environment Study Conducted by Kemnitz et al (Used with permission) [7]

	Pure Argon		$Ar - H_2$	
Laser Speed (mm/s)	O (ppm)	H (ppm)	O (ppm)	H (ppm)
Powder	219	11	-	-
1000	172	5	619	5
400	163	5	693	8
200	130	5	831	5
100	89	5	1027	5

Three-Point-Bend Test Analysis

Maximum Stress

Table 4. ANOVA Results for Maximum Stress Response

Source	Sum of Squares	df	Mean Square	F-value	p-value
Model	2.178E+05	4	54445.69	7.51	0.0006
A-Speed	39337.70	1	39337.70	5.43	0.0294
B-Test Temp	80928.58	1	80928.58	11.16	0.0030
C-H2 %	63508.72	1	63508.72	8.76	0.0072
AB	34007.76	1	34007.76	4.69	0.0414
Residual	1.595E+05	22	7249.96		
Lack of Fit	35988.11	4	8997.03	1.31	0.3034
Pure Error	1.235E+05	18	6861.72		
Cor Total	3.773E+05	26			

Table 4 details the results of the ANOVA analysis on the maximum stress data. The factors which were included in the model all had a p-value of <0.05, and the resulting model fit the data very closely. The single-factor variations of laser speed and test temperature appeared to be highly significant in their own right, but the strength of their significance was likely due to the two-factor interaction of which they were both a part. It is also notable that while a curvature check was conducted, it was not found to be significant. Both this and the fact that no

transform was required to achieve this model, indicates that the relationship between the factors under consideration and the response was relatively linear.

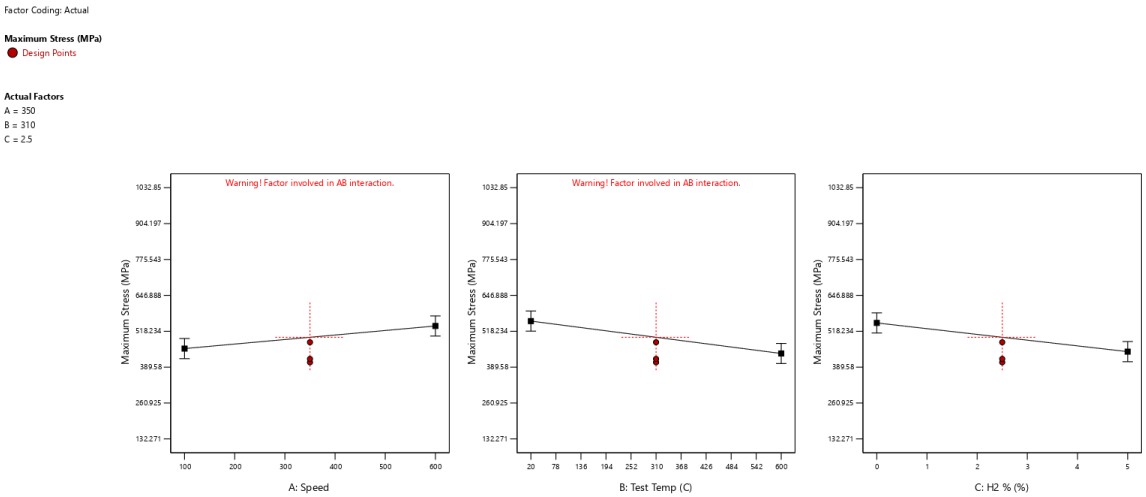

Figure 10. Maximum Stress Response To Significant Factor Variance

As Fig 10 shows, the addition of H_2 to the N_2build atmosphere causes a decrease in material strength. Previous research has shown that atmospheric H_2 contributes to higher-strength W in an inert Ar atmosphere [7]. Here, it is conjectured that introducing H_2 into an N_2-heavy atmosphere instead results in competing reactions between the two gases, reducing the energy available for the primary goal of thoroughly melting the W and possibly forming oxidation at the grain boundaries similar to that observed in previous research on $Ar - H_2$.

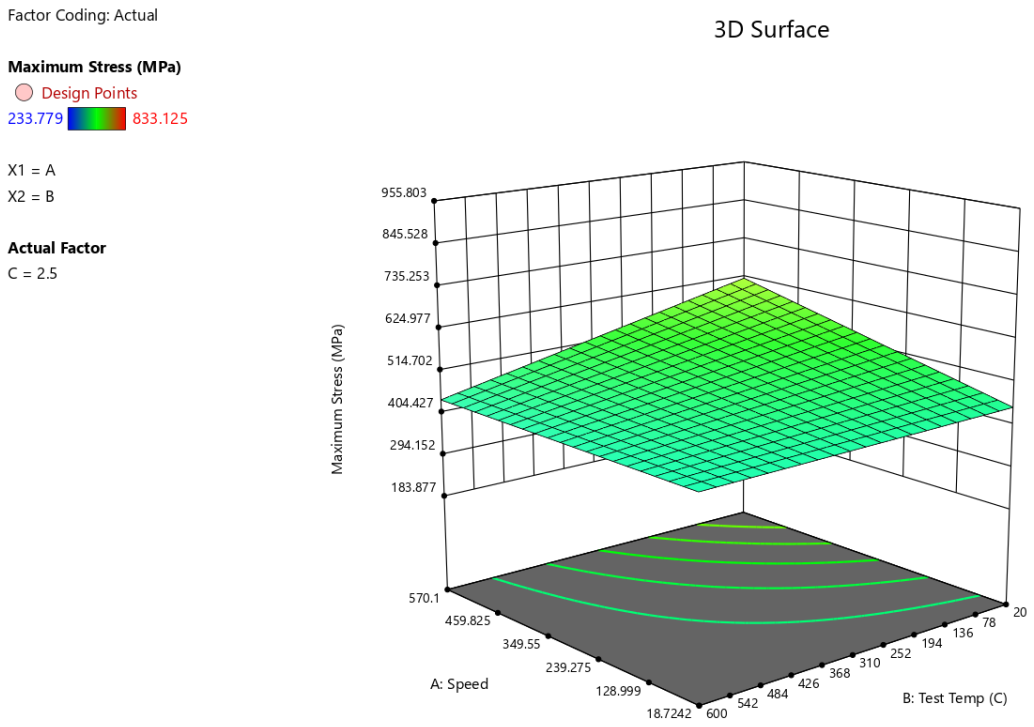

Figure 11. Maximum Stress Response Surface for Two-Factor Interaction Resulting from Atmospheric Variance Experiment

As shown in Fig 11, test temperature influenced the maximum stress response of the material, particularly in concert with speed. While the slope associated with test temperature is shallow, it does trend negatively with increased temperature despite the effects of speed and even seems to largely overwhelm them, resulting in a response surface edge that exhibits the least severe slope present on the surface as a whole. This could indicate that at higher temperatures, the differences in processing speed, and its effect on resulting microstructure and impurities, becomes far less relevant. Further testing at higher temperatures could help determine if this remains valid beyond the scope of the present experiment.

The maximum UTS value achieved was 833.13 MPa, and this specimen was manufactured in the 100% N_2 atmosphere, with a laser speed of 600 mm/s, and tested at room temperature. The range for the strength values collected from the 100% N_2 samples was 397.51-833.13 MPa, which agrees well with the range associated with hot-rolled W rods [21]. Since the range for the hot-rolled rods included a wide variety of different processes and methods to service a multitude of different applications, the results of this experiment could be used to help tailor additively manufactured W parts to a similar range of products.

Break Stress

Table 5. ANOVA Results for Break Stress Response

Source	Sum of Squares	df	Mean Square	F-value	p-value
Model	1026.43	4	256.61	38.28	< 0.0001
A-Speed	16.84	1	16.84	2.51	0.1280
B-Test Temp	818.08	1	818.08	122.03	< 0.0001
C-H2 %	45.27	1	45.27	6.75	0.0168
AB	146.25	1	146.25	21.82	0.0001
Curvature	88.65	1	88.65	13.22	0.0015
Residual	140.78	21	6.70		
Lack of Fit	18.05	3	6.02	0.8824	0.4688
Pure Error	122.73	18	6.82		
Cor Total	1255.86	26			

Unlike the maximum stress response, the break stress model requires a transform to fit the data. The square root transform proved to be the best fit, indicating that the response was parabolic. As might be inferred from this finding, the ANOVA also confirmed that the curvature check was significant in this case. In this model, the only significant single factors were temperature and atmospheric composition, but speed was included to maintain model hierarchy

since the two-factor interaction between speed and temperature was once again significant.

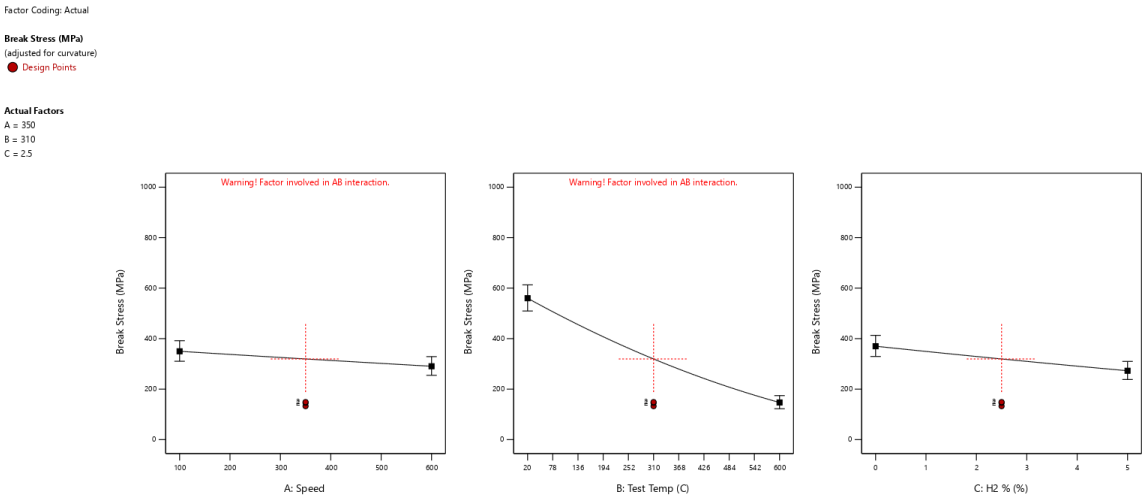

Figure 12. Break Stress Response To Significant Factor Variance

The addition of atmospheric H_2 also negatively impacted break stress, as shown in Fig 12. It is conjectured that once again, the competing reactions between O_2 and the two other gases resulted in greater numbers of secondary-phase particles and pores, causing an overall decrease in the break stress. The chemical analysis and the pore counts support this conclusion.

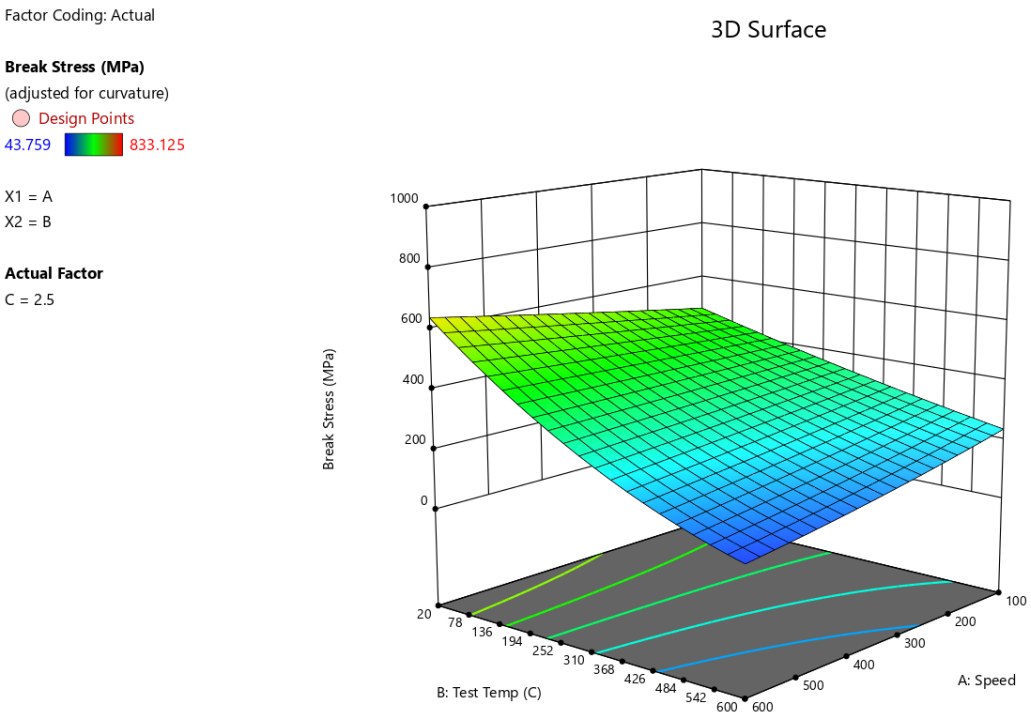

Figure 13. Break Stress Response Surfaces for Two-Factor Interactions Resulting From Atmospheric Variance Experiment

The only two-factor interaction with significant impact on the break stress response surface was that of laser speed and test temperature. While test temperature had a strong negative impact on break stress, the impact of increasing laser speed reversed from increased break stress at room temperature to decreased break stress at 600 ℃. However, the relative impact of laser speed at higher temperatures was decreased, as evidenced by the shallower slope at that edge of the response surface.

Maximum Strain

Table 6. ANOVA Results for Break Stress Response

Source	Sum of Squares	df	Mean Square	F-value	p-value
Model	0.0028	4	0.0007	1155.21	< 0.0001
A-Speed	2.978E-06	1	2.978E-06	4.88	0.0385
B-Test Temp	0.0028	1	0.0028	4565.19	< 0.0001
C-H2 %	4.666E-06	1	4.666E-06	7.64	0.0116
AB	0.0000	1	0.0000	43.13	< 0.0001
Curvature	0.0001	1	0.0001	224.96	< 0.0001
Residual	0.0000	21	6.108E-07		
Lack of Fit	3.362E-06	3	1.121E-06	2.13	0.1318
Pure Error	9.465E-06	18	5.258E-07		
Cor Total	0.0030	26			

The best fit for the maximum strain data was a linear regression model: while curvature was found to be significant, the curve was shallow enough that a parabolic or logarithmic transform would have been an overcorrection. As a result, while the model has a high correlation to the actual data, the lack-of-fit p-value is close to half that of the other two models. While it is closer to being significant than the other two responses, it remains above the threshold for significance. The impact on the effectiveness of the model is that it will be slightly less accurate in its maximum strain predictions towards the center of the design space, but that variance should still be well within the margin of error.

All three single factors were significant contributors to the maximum strain response, but, as indicated by its extremely low p-value, temperature was by far the strongest contributor. It also appears to have heavily influenced the significance of the two-factor interaction between speed and temperature. This was an expected result since there are well-established correlations between the temperature of a metal and its ductility [4].

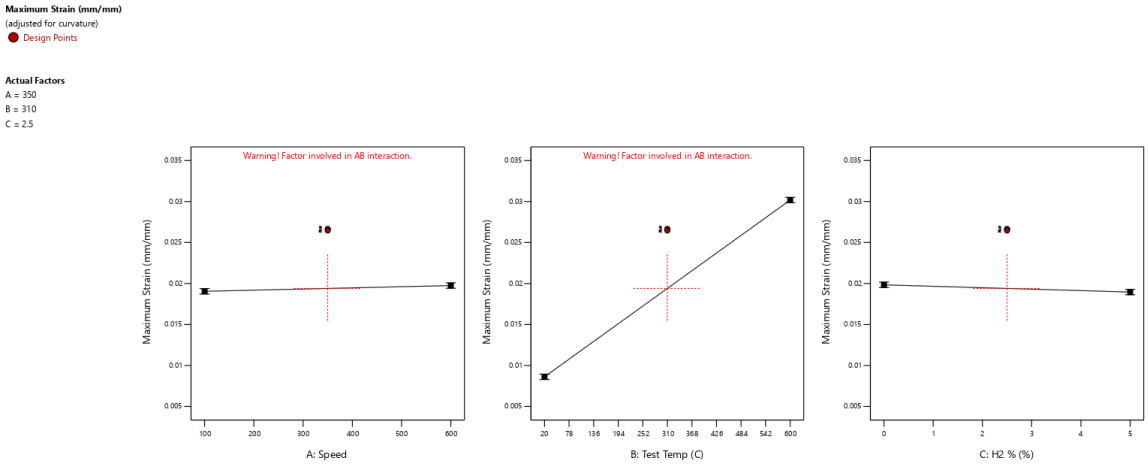

Figure 14. Maximum Strain Response To Significant Factor Variance

Not only was the material strength reduced, but maximum strain was also negatively affected by the introduction of H_2 into the N_2 build atmosphere. Much as the increase in porosity and secondary-phase particles caused a decrease in strength, these properties could also have reduced the material's plasticity by increasing the number of crack initiation sites weakening the material. As tension was applied to the material, the likelihood of dislocation motion prevention, and thus stress concentrations, was greater since there were comparatively more gaps in the material. The increased number of these sites would have forced greater loads on the remaining metallic bonds, and since less material would have been able to slip before the cracks propagated rapidly, the overall maximum strain achievable would have been reduced relative to the samples processed in pure N_2 [29].

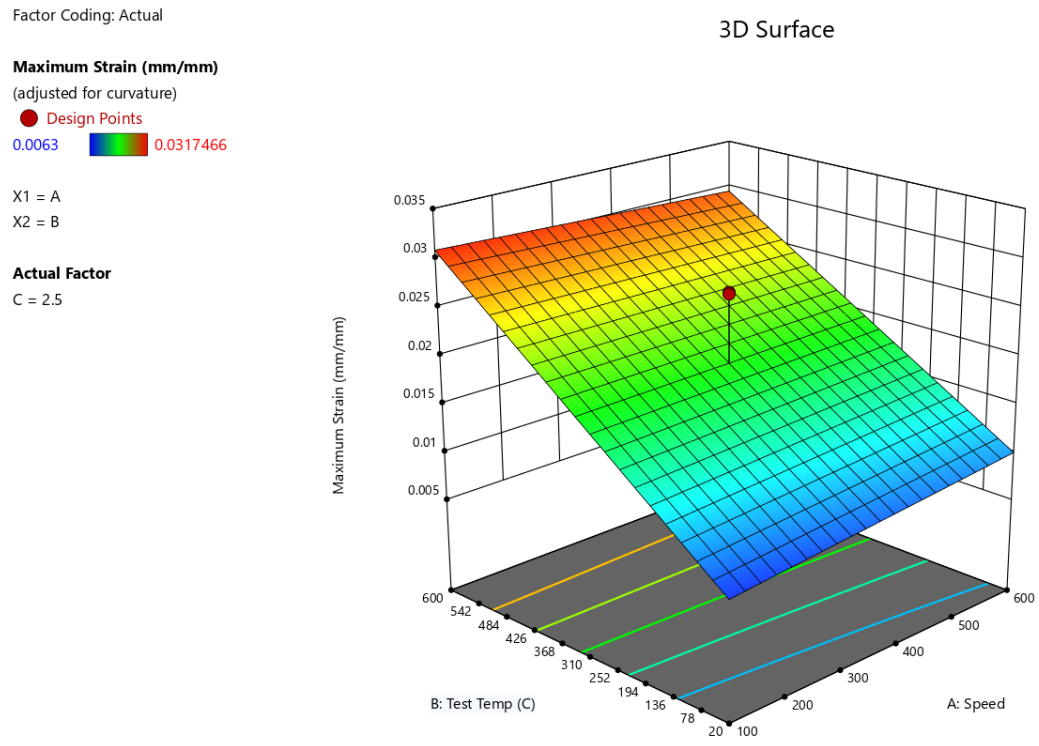

Figure 15. Maximum Strain Response Surfaces for Two-Factor Interactions Resulting From Atmospheric Variance Experiment

Figure 15 shows that the break strain of the material was far more heavily dependent upon the temperature at which the experiment was conducted than on the atmosphere or speed at which it was printed. It also shows that there was a statistically significant interaction between the test temperature and the print speed, but given the slope of the surface, it is reasonable to concur that the driving factor in the interaction was the test temperature, while the laser speed only introduced slight deflections at the corners of the design surface. Given that the projected applications of this material could be subjected to far greater temperatures than 600 ℃, it would be valuable to conduct further testing at higher

temperatures to determine the total temperature range in which the slope of this response surface rises so aggressively.

SEM Imagery

Room Temperature 100% N_2 Fracture Surface

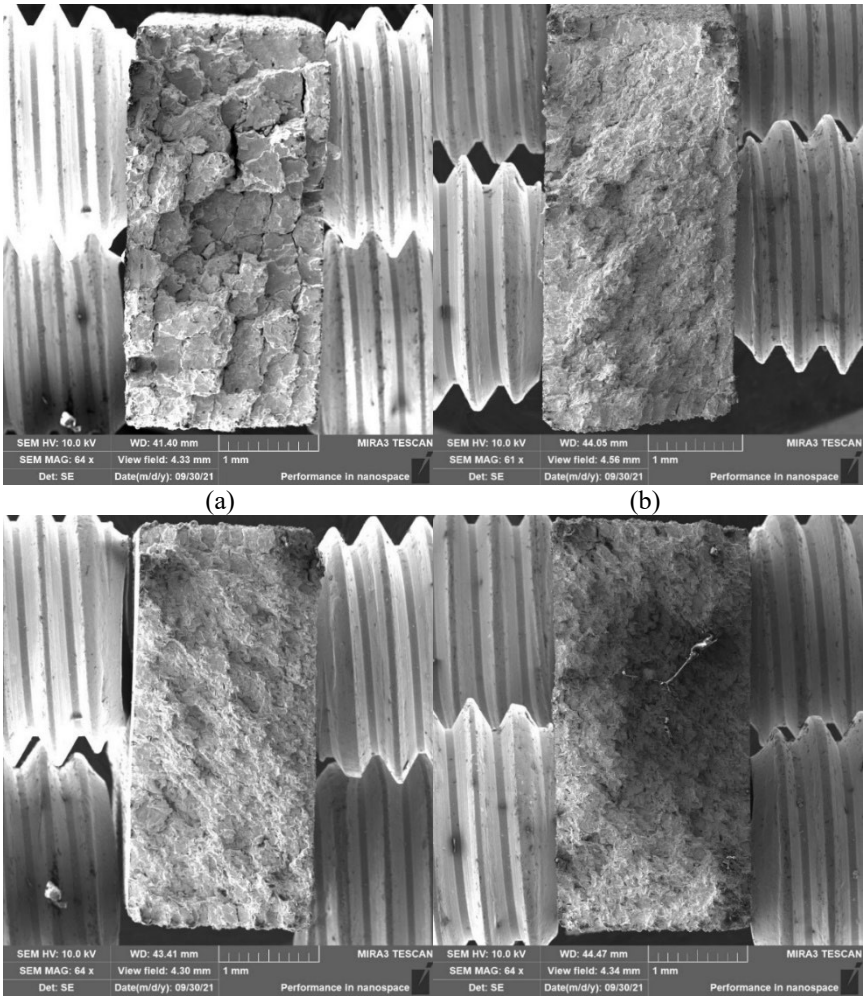

Figure 16. Fracture Surfaces of Samples Processed in 100% N_2 at 100 mm/s (a), 200 mm/s (b), 400 mm/s (c), and 600 mm/s (d), Subjected to Room Temperature Three-Point Bend Testing

Figure 16 shows the broken cross-sections of the vertically printed pure W manufactured in the pure nitrogen atmosphere. The fracture surfaces propagated perpendicular to the build direction transverse to the orientation of the columnar

grains. The 100 mm/s sample processed in N_2, shown in Fig 4.7(a), displayed notably larger columnar structures in the build direction than was exhibited by any of the faster speeds. These formations were large enough to be visible to the naked eye. The faster laser processing speeds, on the other hand, most clearly display the 45° weld track pattern. This seems to indicate that there is a critical amount of energy necessary to form the larger columns that is reached while manufacturing the 100 mm/s sample but not by the 200 mm/s and faster samples. From the ANOVA analysis, the presence of these large columnar structures corresponds to weaker and less ductile metal. This could be due to the apparent lack of cohesion between these structures evidenced by large cracks and separation. This separation may have caused the metal to behave more like a composite with metal fibers and a weaker, secondary particle matrix [30]. Alternatively, the weak cohesion between the large columnar structures may have facilitated easy crack propagation along their boundaries resulting in weak and brittle material behavior.

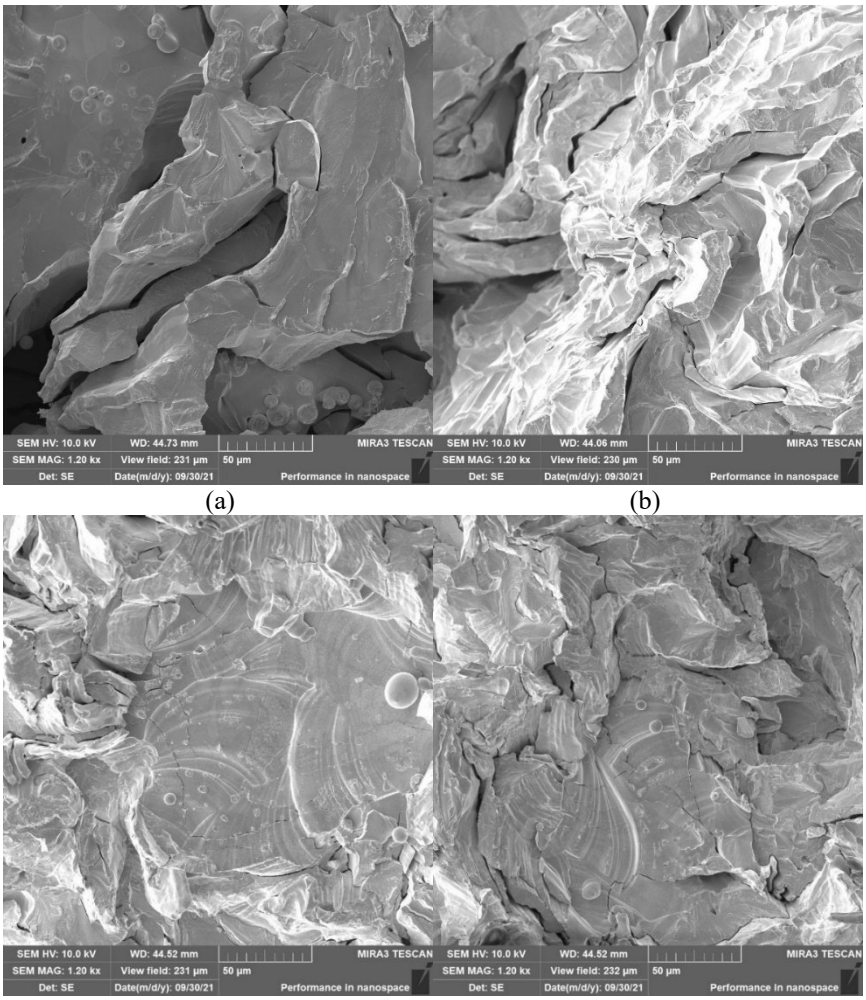

Figure 17. Fracture Surfaces of Samples Processed in 100% N_2 at 100 mm/s (a), 200 mm/s (b), 400 mm/s (c), and 600 mm/s (d), Subjected to Room Temperature Three-Point Bend Testing at 1.2kx Magnification

At 1.2kx magnification, shown in Fig 17, evidence of brittle transgranular fracture in the form of river patterns are visible in all photographed samples. This was expected, given that W is brittle at room temperature [4]. However, there are notable differences in the samples at different speeds. The 100 mm/s sample exhibits the largest and cleanest fracture planes and provides the clearest view of the grain structure. The intergranular cracks present between the fracture planes were also the largest at the slowest speeds. This was likely due to the lack of

stress relief cracks within the large columnar structures. The grains internal to the columns seem to have had such excellent cohesion that separation could only occur at column boundaries. The large-scale cracking between the columns may also have resulted from large misorientation angles between grains in neighboring columns, which caused poor bonding.

The faster laser speeds seem to show far greater grain misalignment, resulting in much smaller planar surfaces at the crack face. There are also more cracks internal to these planes and more evidence of secondary-phase particles present on them, these primarily showing on the 400 mm/s and 600 mm/s samples.

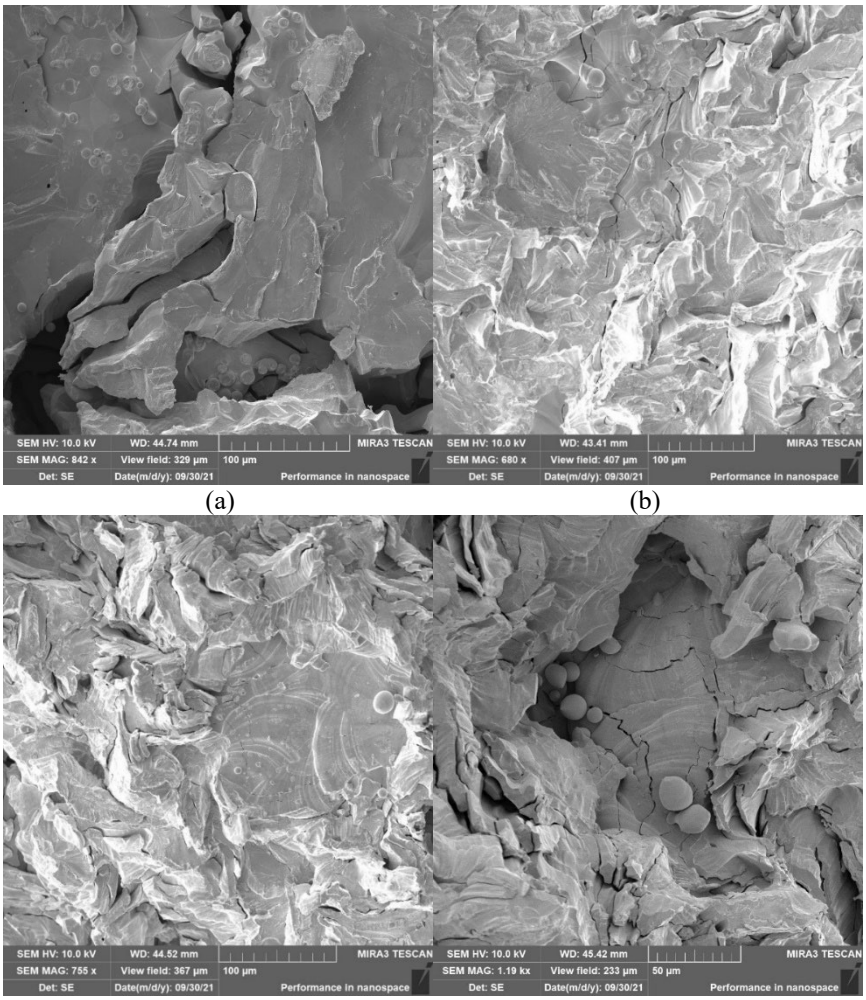

Figure 18. Relative Amount of Unmelted Powder Present at Fracture Surfaces of Samples Processed in 100% N_2 at 100 mm/s (a), 200 mm/s (b), 400 mm/s (c), and 600 mm/s (d), Subjected to Room Temperature Three-Point Bend Testing

Figure 18 provides sample views of the amount of unmelted powder at each speed. The mid-range speeds appear to have the least amount of unmelted powder, while the extremes exhibit slightly more. However, all speeds showed relatively little sign compared to the other tested atmospheric conditions. This observation, combined with the relatively scant presence of secondary-phase particle deposits, seems to indicate that the N_2-heavy atmosphere required little

energy from the overall system, and the majority could therefore be directed at the intended W powder target.

There are several conjectures to make regarding why the 100 mm/s and 600 mm/s samples contained more unmelted powder. Given that 600 mm/s was the fastest extreme of the speed range, it is most probable that insufficient energy was provided to the sample due to the shortness of the laser dwell time. This has been shown in previous studies to be a significant factor [6,7,8] and therefore seems to be the most reasonable cause. However, since the 200 mm/s and 400 mm/s samples seem to have received sufficient energy, it is unlikely that short dwell time is the culprit in the 100 mm/s case. Due to the significant lack of oxides and other secondary phases present on this sample, it is proposed that enough energy was provided by the laser to reach the formation energy for reactions between the N_2 and trace amounts of O_2 in the atmosphere. If this is the case, that could have prevented the full complement of the energy from acting on the W powder, resulting in incomplete melting.

This idea is supported by the fact that the powder particles present almost uniformly exhibit signs of having partially melted before something, (conjectured to be O impurities from powder manufacture) erupted from within the spheres. It is theorized that the melting of these powder particles then ceased due to the energy being instead used in the $N_2 - O_2$ reaction. This would also prevent the formation of WO_3, since the O_2 required would have reacted with the N_2 instead.

Alternatively, these unmelted powder particles could have been transported from elsewhere in the powder bed during sintering via spattering [31].

The ruptured surfaces may have resulted from gases building up between the grain boundaries internal to the powder particle and attaining sufficient energy to rupture the particle surface but not completely melt. Then, upon the powder particle landing on the more completely melted surface elsewhere on the sample, the still-hot powder particle semi-adhered there.

Room Temperature 2.5%H_2 Fracture Surface

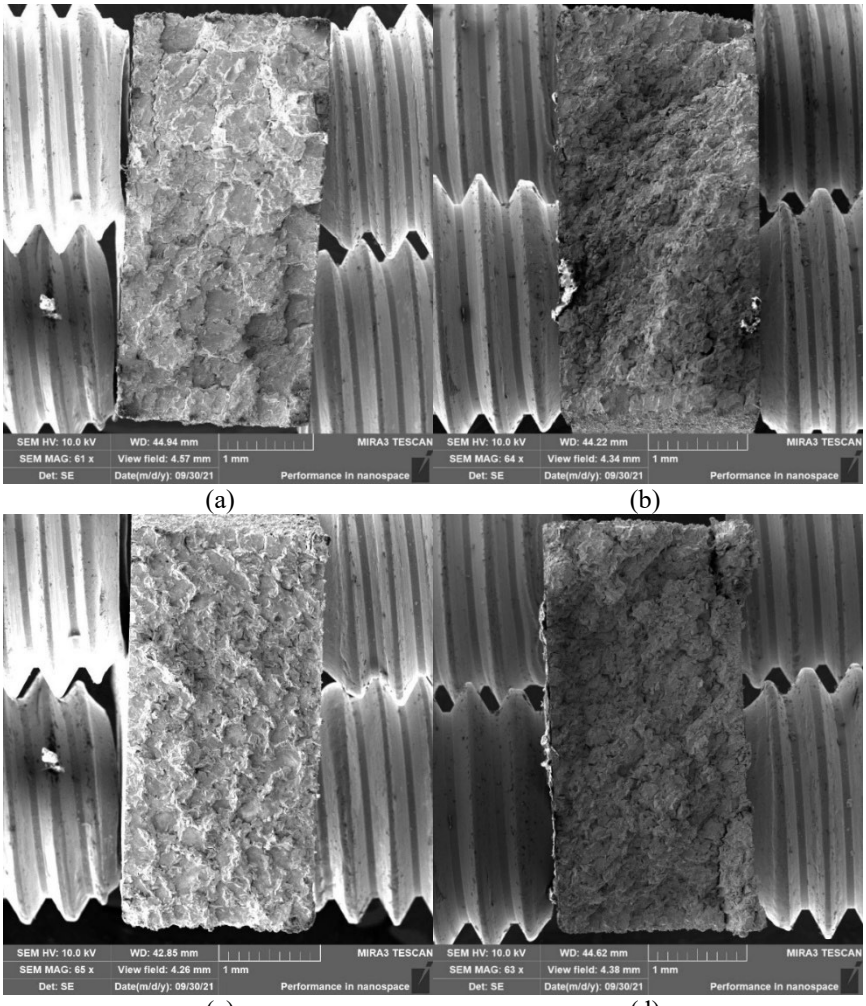

Figure 19. Fracture Surfaces of Samples Processed in 2.5% H_2 at 100 mm/s (a), 200 mm/s (b), 400 mm/s (c), and 600 mm/s (d), Subjected to Room Temperature Three-Point Bend Testing

The fracture surfaces shown in Fig 19 generally follow the trend established in the samples processed in 100% N_2. Once again, the 100 mm/s sample has large, macroscopically visible columnar structures in the build direction, while the faster speeds do not. The columnar structures appear smaller and less defined than in the pure nitrogen environment, and the 45° weld tracks, while still observable, are less identifiable. The cracks between the columns also appeared less pronounced than in the previous sample set.

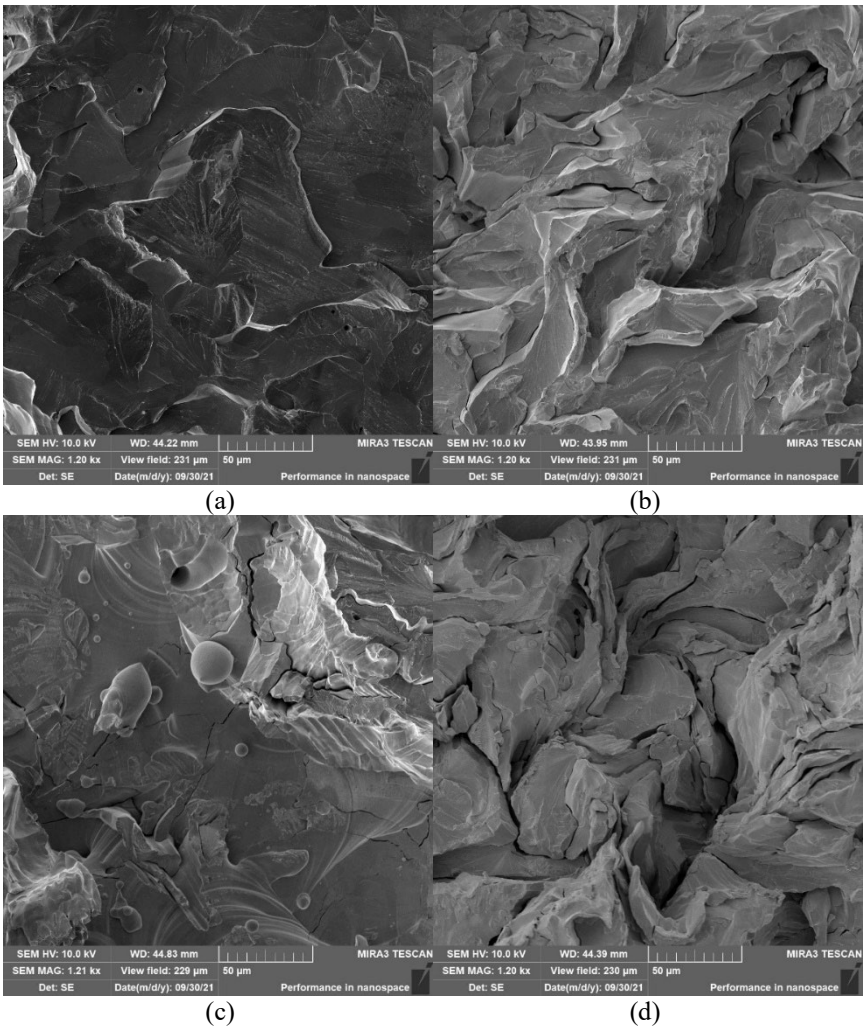

Figure 20. Fracture Surfaces of Samples Processed in 2.5% H_2 at 100 mm/s (a), 200 mm/s (b), 400 mm/s (c), and 600 mm/s (d), Subjected to Room Temperature Three-Point Bend Testing at 1.2kx Magnification

The fracture surfaces of these samples show river patterns and clear fracture planes, indicating that these too experienced transgranular brittle fracture. However, whereas the 100 mm/s sample in 100% N_2 had large cracks in between columns and notably large and smooth fracture planes, the 2.5% H_2 sample has far fewer and smaller cracks and a more uneven fracture face. The 200 mm/s and 400 mm/s samples appear relatively similar to their 100%-N_2 counterparts, but the 600 mm/s sample is significantly different, more closely resembling the 200 mm/s sample in its set, whereas the 600 mm/s sample processed in 100% N_2 was nearly identical to the 400 mm/s sample in that set. It is conjectured that this is related to the introduction of the $H_2 - O_2$ reaction, which caused the amount of energy available for the sintering process to varying by instead using a percentage of the available laser energy to create water vapor.

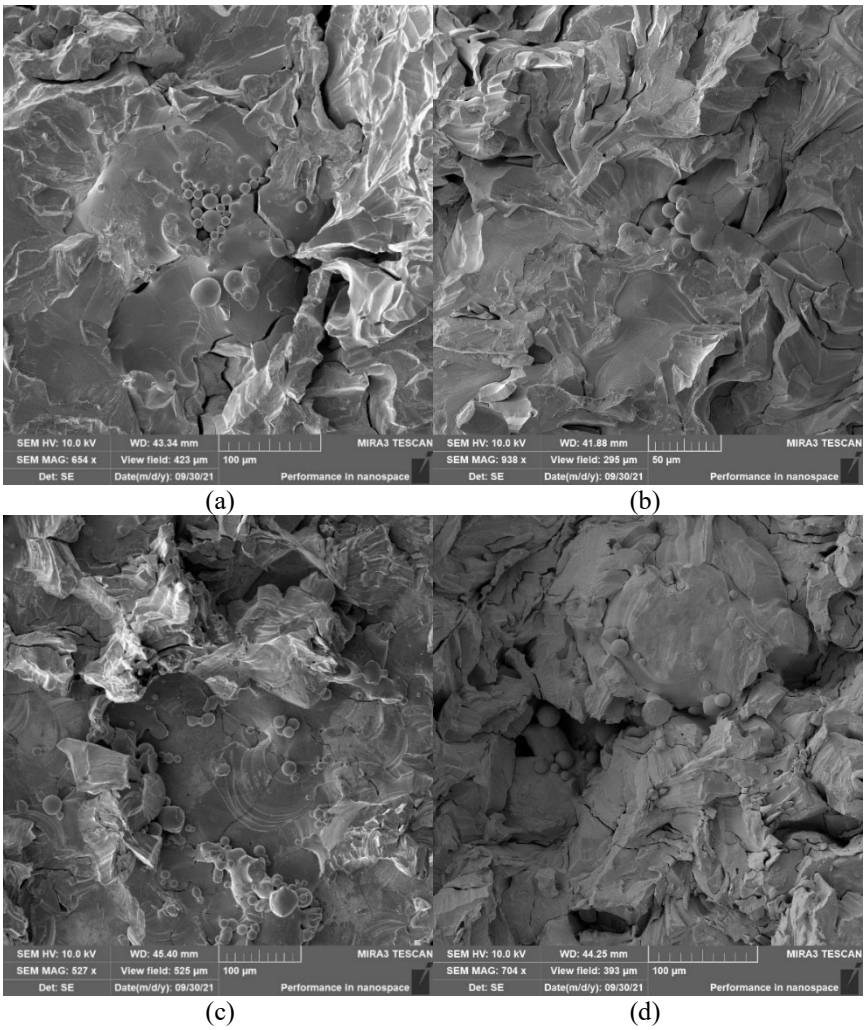

Figure 21. Relative Amount of Unmelted Powder Present at Fracture Surfaces of Samples Processed in 2.5% H_2 at 100 mm/s (a), 200 mm/s (b), 400 mm/s (c), and 600 mm/s (d), Subjected to Room Temperature Three-Point Bend Testing

Unlike the samples processed in 100% N_2, the unmelted powder present in the 2.5% H_2-atmosphere samples is relatively uniform in both amount and appearance. The 100 mm/s and 400- mm/s cases are arguably more similar, as are the 200 mm/s and 600 mm/s cases, but there do not appear to be any of the ruptured spheres that were present in the 100 mm/s 100% N_2 sample. All samples also show evidence of secondary-phase particles.

It is theorized that the energy that would otherwise have gone to fully melting the powder was partially consumed in the competing reactions between N_2 and O_2 and H_2 and O_2. This is supported by the apparent uneven melting visible in particularly the 200 mm/s and 600 mm/s articles. The relatively small amounts of O_2 would be consumed rapidly in reactions with either N_2 or H_2, which would cause erratic fluctuations in the energy available for melting. This would result in nonuniform structures and equally complex cracking in an effort to balance the internal stress concentrations forming in the material. It is also hypothesized that the presence of secondary-phase particles visible on the fracture surfaces could be due to the competing reactions causing trace amounts of O_2 or O to break free from their bonds and be projected towards the W with enough energy to result in WO_3, which would then have collected at the grain boundaries and weakened them.

It is postulated that one of the causes of increased spattering could have been the introduction of competing atmospheric reactions. The different reaction rates of N_2 and H_2 with O_2 could have resulted in much more chaotic O atom of varying energy colliding with the W melt pool [32], which would have resulted in greater likelihood of spattering as a result.

There also could have been an increase in spattering due to the competitive reactions between N_2 and H_2. The rapid forward and reverse reactions resulting from energy transfers and molecular collisions could have liberated O atoms who would then have collided with the molten W, increasing the energy in that part of the system and thus causing more spattering as a result.

Room Temperature 5%H_2 Fracture Surface

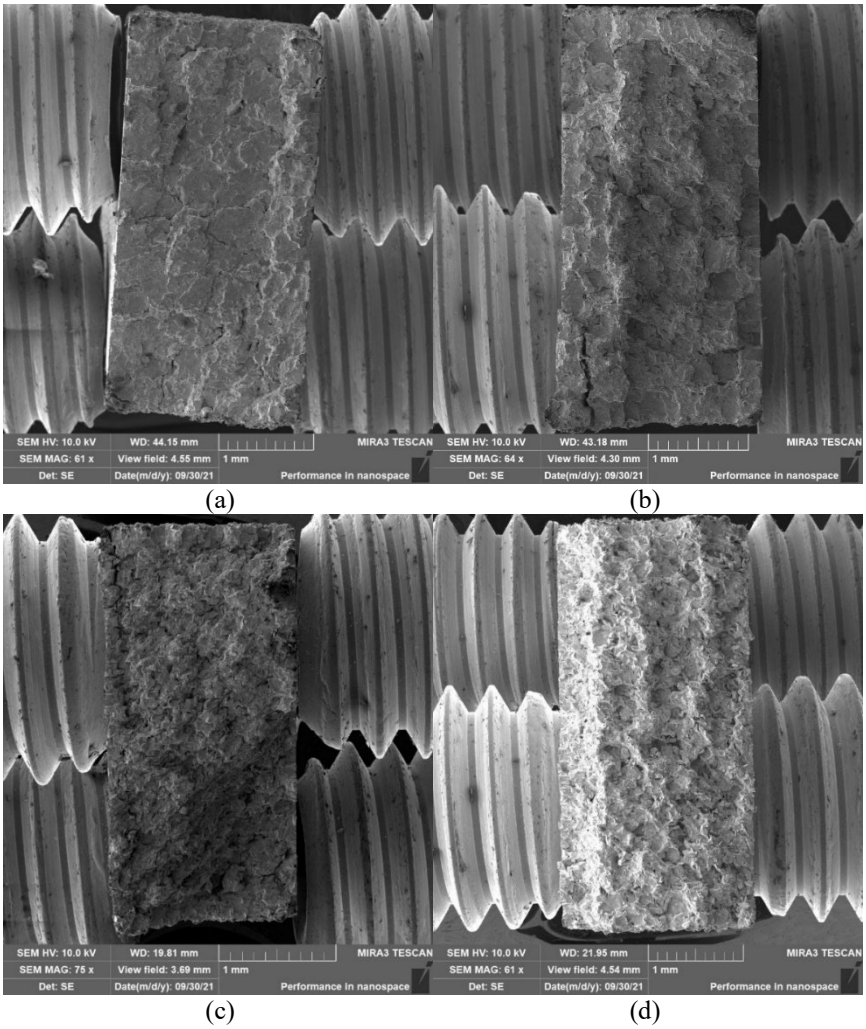

Figure 22. Fracture Surfaces of Samples Processed in 5% H_2 at 100 mm/s (a), 200 mm/s (b), 400 mm/s (c), and 600 mm/s (d), Subjected to Room Temperature Three-Point Bend Testing

The samples shown in Fig 22 again echo the trends noted in those processed in the previous atmospheres to some extent. In this case, however, the 200 mm/s sample appears to exhibit some of the columnar structures previously noted in the 100 mm/s samples rather than entirely adhering to its behavior in the other two processing atmospheres. The separation between the visible columnar structures also appears to be less pronounced.

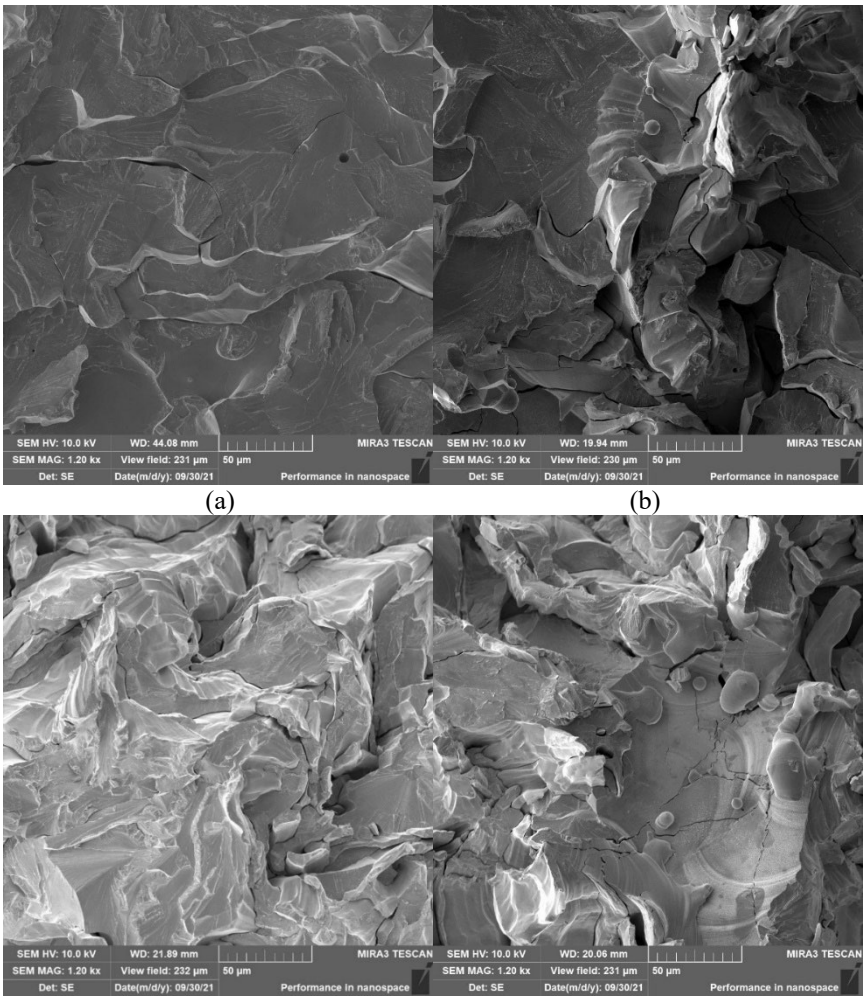

Figure 23. Fracture Surfaces of Samples Processed in 5% H_2 at 100 mm/s (a), 200 mm/s (b), 400 mm/s (c), and 600 mm/s (d), Subjected to Room Temperature Three-Point Bend Testing at 1.2kx Magnification

Figure 23 once again exhibits signs of brittle transgranular fracture evidenced by the presence of river patterns and sharp, angular crack planes. Also, in keeping with the two previous atmospheres, the fracture face generally increased in roughness as the laser speed was increased. The amount and size of stress cracking also closely resembled that present in the 2.5% H_2 case.

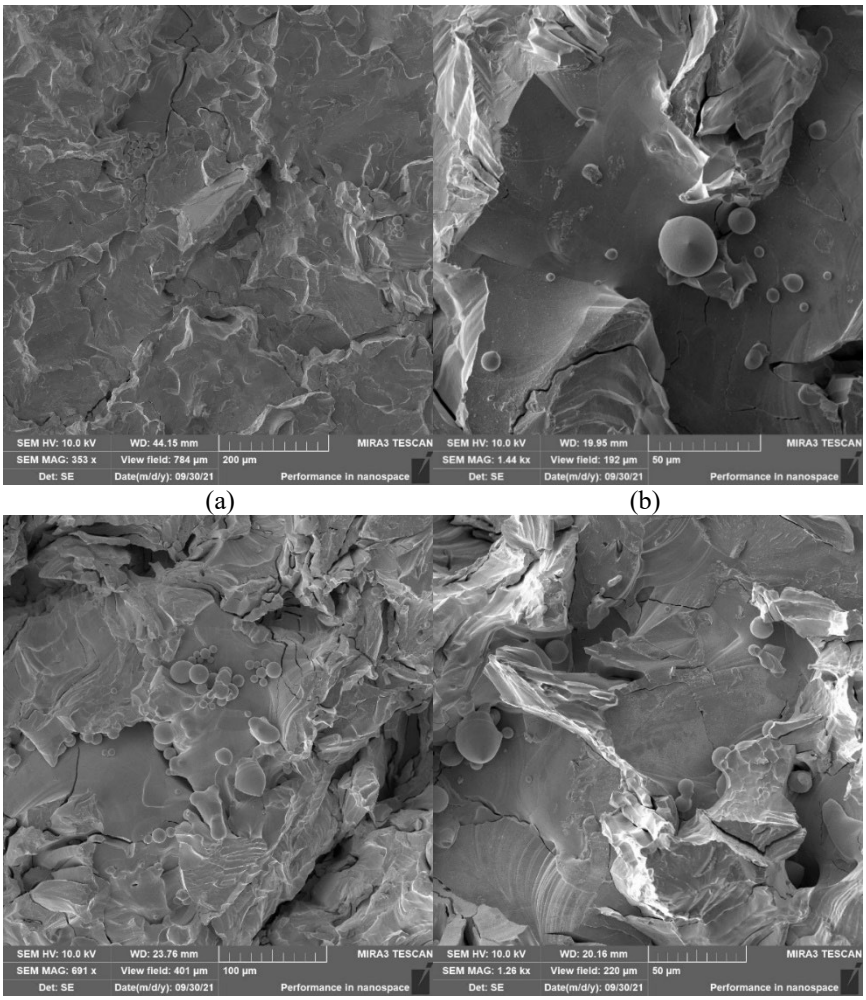

Figure 24. Relative Amount of Unmelted Powder Present at Fracture Surfaces of Samples Processed in 5% H_2 at 100 mm/s (a), 200 mm/s (b), 400 mm/s (c), and 600 mm/s (d), Subjected to Room Temperature Three-Point Bend Testing

There appeared to be a small increase in the number of unmelted powder particles present on the crack surfaces of all four tested speeds, as shown in Fig 24. However, as in the 2.5% H_2 case, the amount of powder present does not appreciably vary between the sample speeds processed at 5% H_2. This is likely again because some of the energy required to melt the particles was instead used to fuel atmospheric reactions. The amount of secondary-phase particles also

appears relatively consistent amongst this group of samples as well as similar to the amount present in the 2.5% H_2 atmosphere case. This seems to indicate that no further increase in oxidation occurs as the percentage of atmospheric H_2 present increases.

600 ℃ 100% N_2 Fracture Surface

The samples tested at 600 ℃ looked the same as those tested at room temperature at low magnification because they were all processed in the same way. The changes to the material caused by increased temperature were apparent and higher magnification, however.

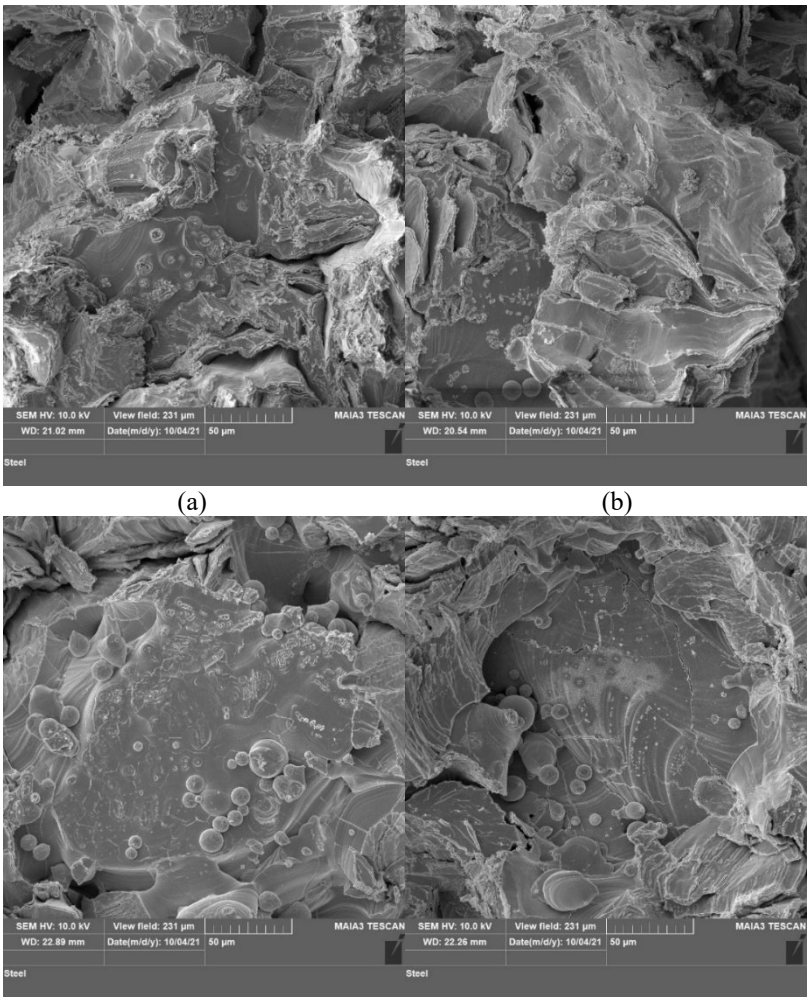

Figure 25. Fracture Surfaces of Samples Processed in 100% N_2 at 100 mm/s (a), 200 mm/s (b), 400 mm/s (c), and 600 mm/s (d), Subjected to Three-Point Bend Testing at 600 ℃ at 1.2kx Magnification

As seen in Fig 25, all samples again primarily exhibited evidence of brittle trans- and intergranular failure. Since the DBTT of W is 400 ℃, [4] this was

unexpected, but there is a possible explanation based on previous studies. It has been posited that the presence of oxides in W increases the DBTT to a much higher value than 400 ℃, [16] so it is most likely that the DBTT of these samples had been affected by oxidation. Thus, 600 ℃ was probably an insufficient temperature to achieve the amount of ductility expected.

While the fracture types appeared relatively unchanged, there were visible changes to the fracture surfaces that were exposed to this higher test temperature. All samples appeared to be covered in a layer of secondary phase particles on the exposed fracture surfaces. These layers were generally thin enough that they did not obscure the general form of the W beneath them, and as such, it can be seen that testing at this temperature does not seem to have had a large-scale effect on the overall shape or structures of the samples at this level of magnification. The one significant caveat to this statement is that the secondary phase layer does prevent the underlying grain structure of the fracture planes from being visible, so no definitive statement can be made regarding the grain sizes or differences in their appearance.

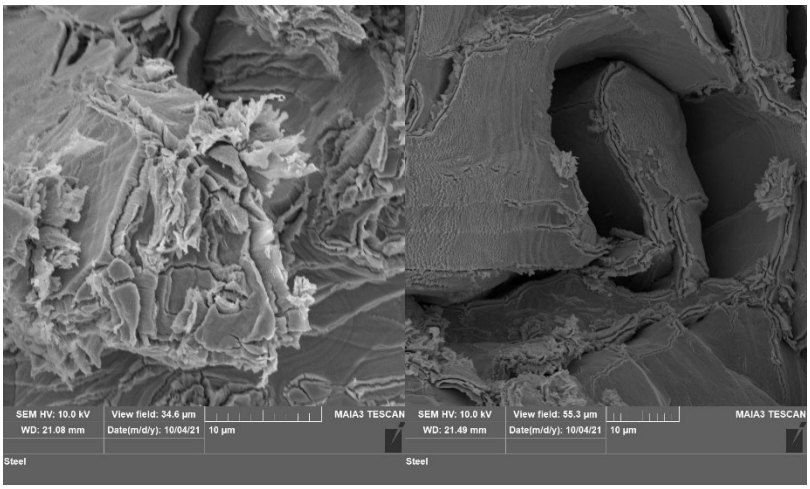

Figure 26. Close Magnification of Dendritic Structures on the Fracture Surfaces

The layers likely consist of a mixture of precipitates, including both byproducts from reactions occurring in the atmosphere internal to the oven, which was atmospheric air, and some level of W oxidation. Based on the findings from previous research, the most likely oxides present were WO_3 and WO_2 [4,13,18,19]. WO_3 is known to readily form at temperatures between $500℃ - 800℃$, making it the most likely oxide to be present, particularly on the fracture surface, which was exposed to $> 500℃$ conditions for several minutes during test apparatus cooldown. Formations concurrent with these oxides can be seen in Fig 26 and have been identified via comparison to similar examples of oxide formations from previous studies. Upon close magnification, the coral-like appearance mentioned in the paper by Venables et al seemed to align well with the formations visible in the collected images seen in Fig 26 [14].

Since high-temperature and high-speed applications are being considered for additively manufactured W, the presence of these precipitates is notable. Generally, the accumulation of oxidation or scale on the surface of a part is

considered detrimental since it could contribute to corrosion and also result in the secondary-phase particles sloughing off of these surfaces and contaminating other parts of the mechanism of which they are a part. However, in high-temperature, high-speed environments, material erosion and ablation is often expected: Usually, the structure of such an article is covered by a layer of sacrificial ablative coating [33]. This is, in fact, one of the reasons that many articles designed for such an environment are single-use.

Unfortunately, WO_3 is known to sublime at temperatures in excess of $800℃$ [4]. This could cause deterioration of the exposed surface at temperatures beyond the scope of this experiment, resulting in decreased load capacity for a given W structure. Further testing at higher temperatures would be necessary to determine the severity of this degradation.

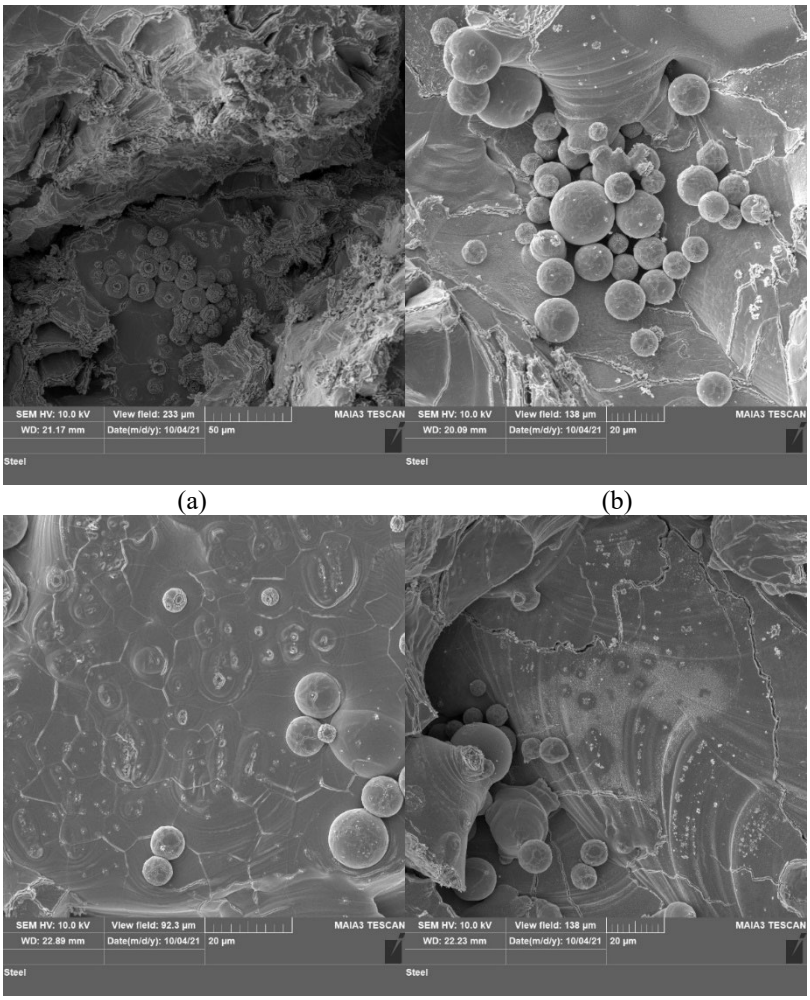

Figure 27. Relative Amount of Unmelted Powder Present at Fracture Surfaces of Samples Processed in 100% N_2 at 100 mm/s (a), 200 mm/s (b), 400 mm/s (c), and 600 mm/s (d), Subjected to Three-Point Bend Testing at 600 ℃

Another noticeable difference between the room-temperature tested samples and those tested at 600 ℃ was the condition of the unmelted powder particles, which are shown in Fig 27. These images show that nearly all unmelted and even some of the partially melted particles present at the fracture surfaces shown major signs of cracking or rupture: some even appear to have almost completely shattered. The level of disintegration on any given sample did not

appear to be a function of atmosphere or laser sintering speed, varying independently of both and even across the fracture surface of a single sample.

It is therefore conjectured that these powder particles were deformed by internal pressure due to gases trapped within the powder during its manufacture. It is unlikely that the particles themselves melted since W has a melting temperature of 3422 ℃ [4], but the 600 ℃ they were subjected to over the course of the experiment could have been enough to excite the pockets of gas internal to the powder to expand with sufficient pressure to rupture the powder particles, whereas the fractions of a second in which they were subjected to the laser during sintering was not. The fact that some signs of similar behavior (shown in Fig 24) was observed in the room-temperature three-point-bend samples with the longest laser dwell time could lend credence to this idea.

The ruptured powder particles appear to be covered in the same layer of secondary phase particles as the rest of the material, but this layer does not seem to be present on the surfaces that would have been internal to the particle prior to rupture. This would indicate that the powder ruptures occurred after the reactions resulting in the layer of precipitates had ceased.

600 ℃ 2.5%H_2 Fracture Surface

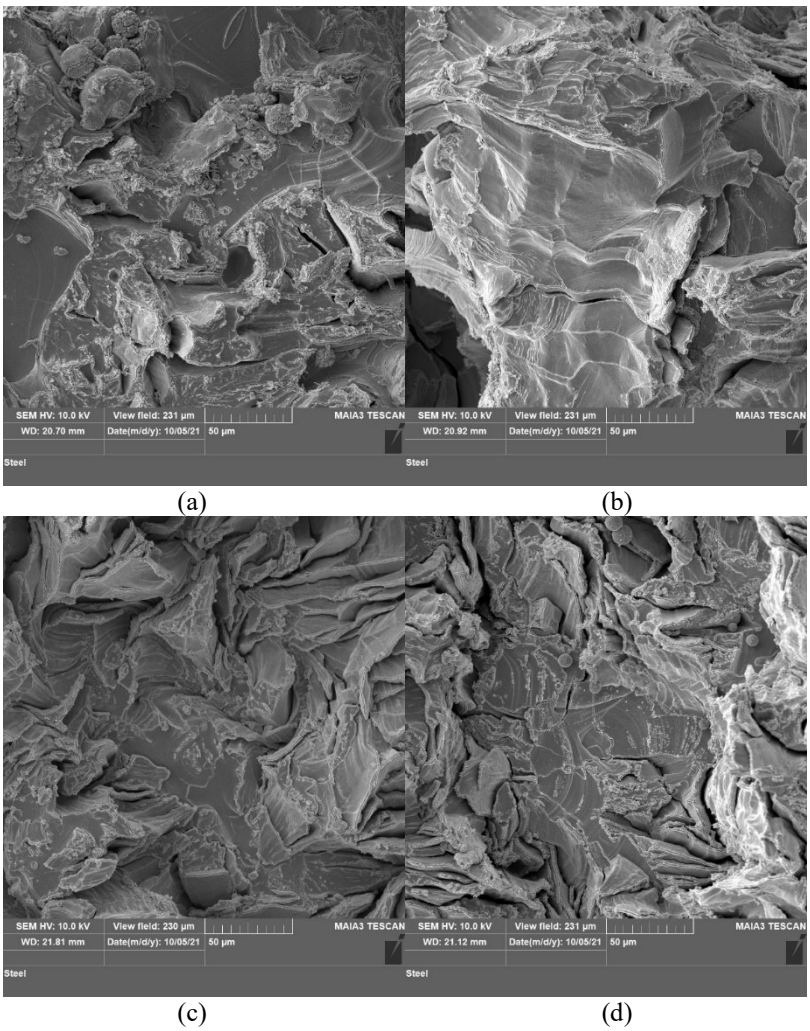

Figure 28. Fracture Surfaces of Samples Processed in 2.5% H_2 at 100 mm/s (a), 200 mm/s (b), 400 mm/s (c), and 600 mm/s (d), Subjected to Three-Point Bend Testing at 600 ℃ at 1.2kx Magnification

The level of oxidation present on the fracture surfaces in Fig 28 did not appear visibly different to that found on the 100%-N_2 samples, supporting the idea that these oxides formed due to the combination of the air in the test chamber and the test temperature rather than due to any significant increase or decrease in constituent O within the samples themselves. This could also be due to any possible differences due to the markedly low O content reported in the chemical

analysis being obscured by the effects of the atmospheric O_2 in the test chamber. Since the target applications of this material would largely occur in chemically reactive atmospheric air, the differences between the build atmosphere compositions in this case may not be the driving factor in determining part survivability.

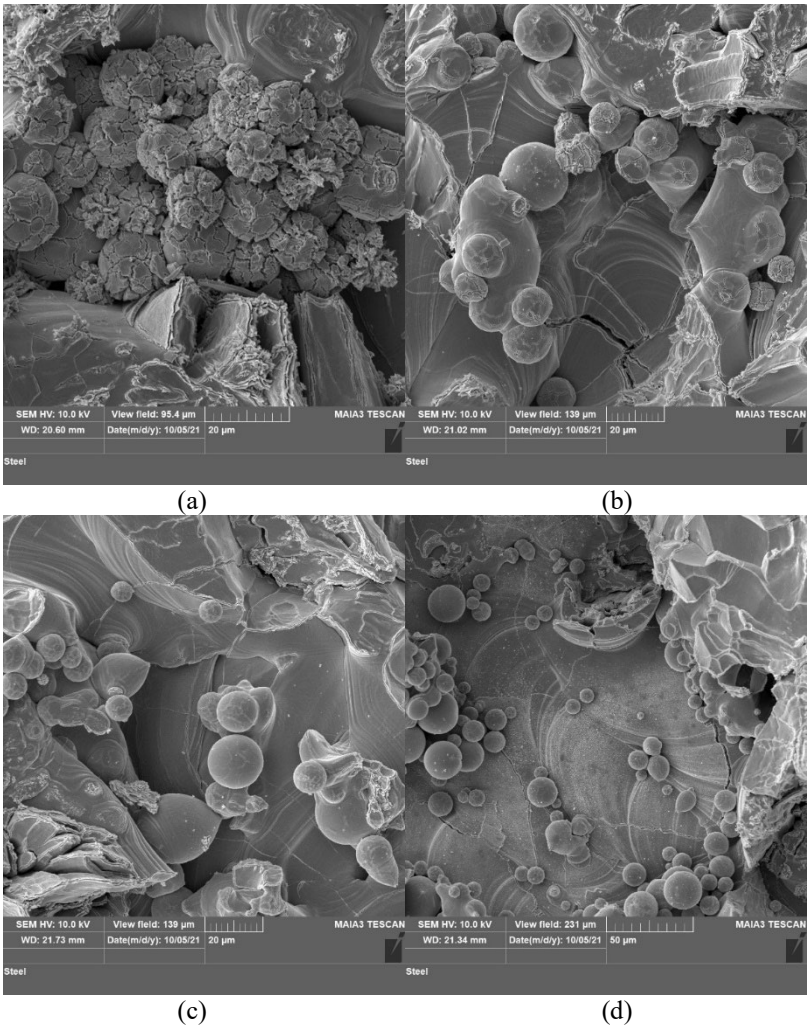

Figure 29. Relative Amount of Unmelted Powder Present at Fracture Surfaces of Samples Processed in 2.5% H_2 at 100 mm/s (a), 200 mm/s (b), 400 mm/s (c), and 600 mm/s (d), Subjected to Three-Point Bend Testing at 600 ℃

The build atmosphere also seemed to have little effect on the condition of the unmelted powder visible on the fracture surface, shown in Fig 29. The same type of rupture along the grains internal to the powder appeared to have occurred as did in the case of the 100%-N_2 build atmosphere samples. In the slowest-speed cases, there did appear to be cases of more violent rupture than were present on the 100% N_2 specimens, however. This could have been due to the presence of a greater amount of secondary particles or gases trapped within those unmelted powder particles, but this would more likely be due to the powder's manufacturing process than to the SLM process.

600 ℃ 5%H_2 Fracture Surface

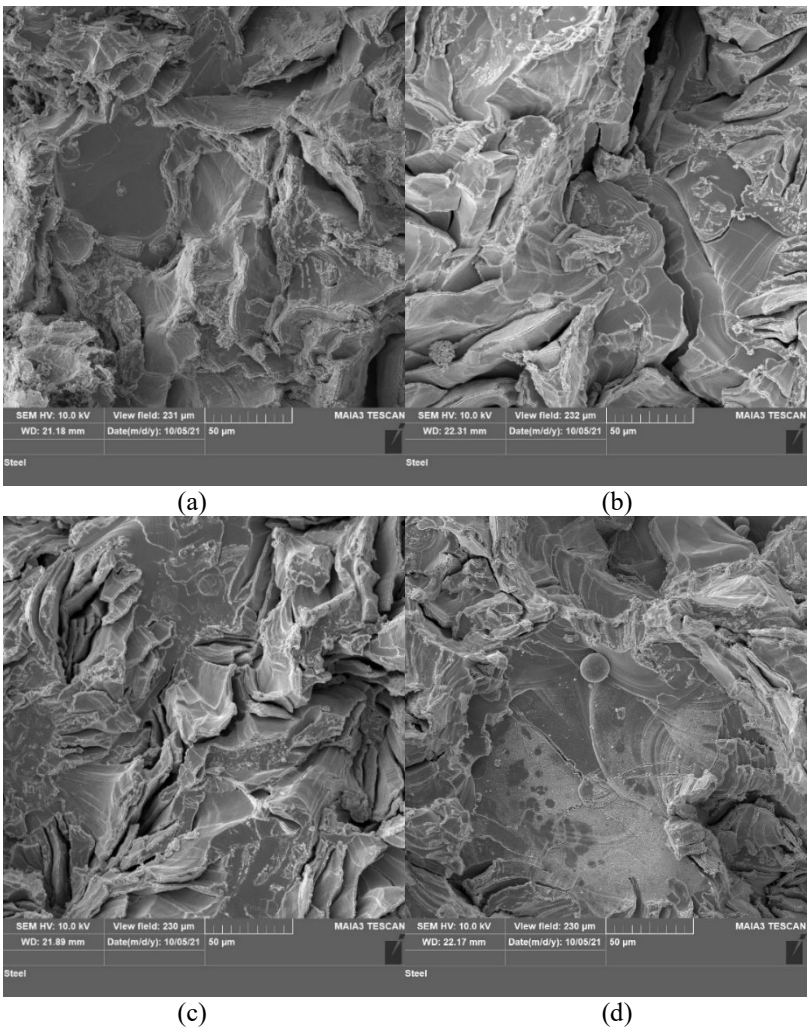

Figure 30. Fracture Surfaces of Samples Processed in 5% H_2 at 100 mm/s (a), 200 mm/s (b), 400 mm/s (c), and 600 mm/s (d), Subjected to Three-Point Bend Testing at 600 ℃ at 1.2kx Magnification

The imaging of the 5% H_2 samples again showed oxidation amounts and types similar to those found in the previous sample batches, as seen in Fig 30 above. It again appeared that oxidation formed on the exposed surface after fracture, as is evidenced by the presence of brittle inter- and trans-granular fracture patterns still visible under the layer of oxide.

Optical Microscopy

Visible light microscopy was also conducted on the samples perpendicular to the build direction and was primarily used to examine relative grain size, relative pore size, and pore number.

100% N_2 Sample Pores

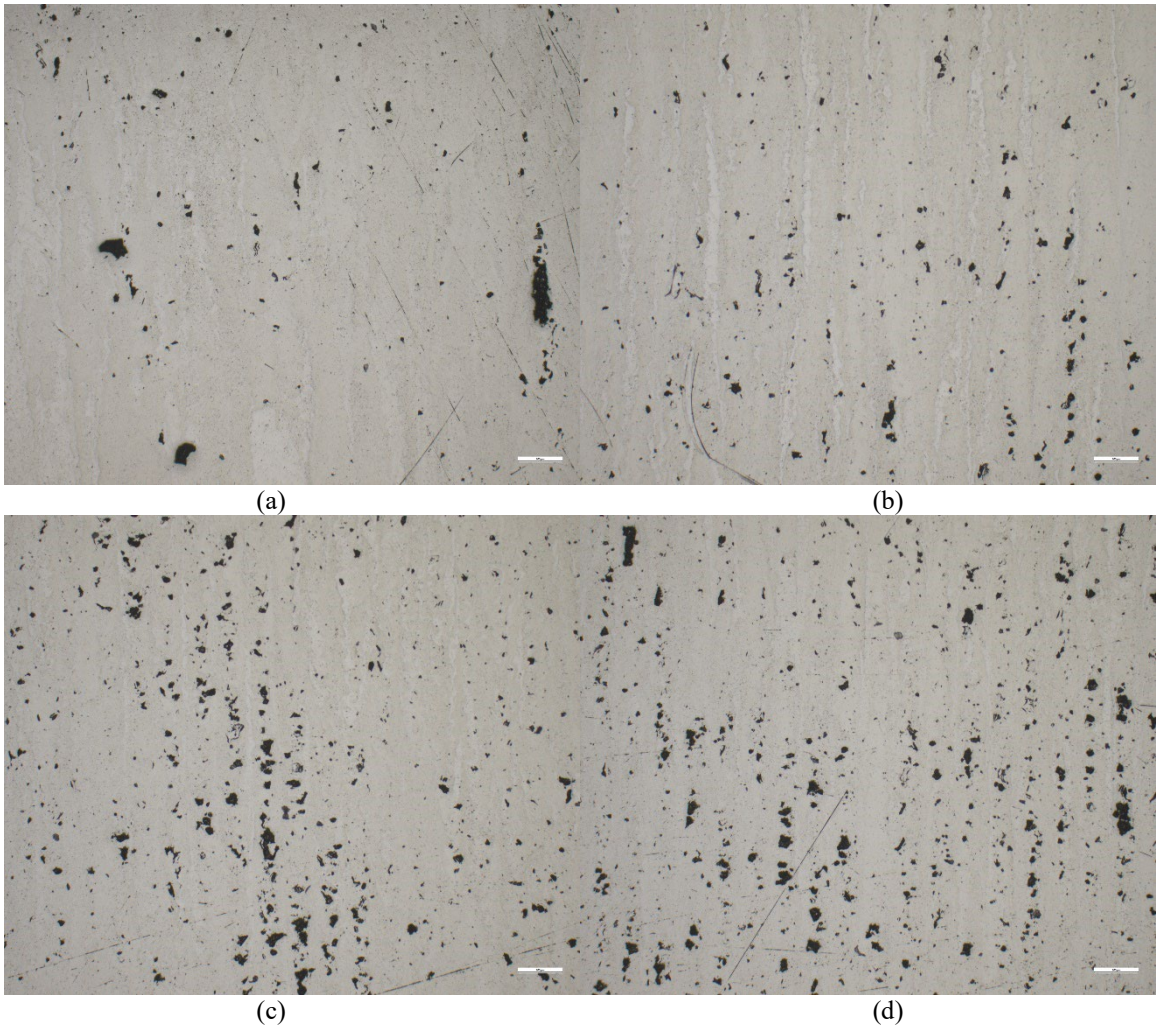

(a) (b)

(c) (d)

Figure 31. Samples Processed in 100% N_2 at 100 mm/s (a), 200 mm/s (b), 400 mm/s (c), and 600 mm/s (d), at 5x Magnification

One of the most prominent observations that was made from the microscopic imaging was that, in general, as laser speed increase, the number and

orderliness of the pores in the material also increased. As Fig 31a shows, in the slowest-speed case, the pores that were present may have been relatively large compared to the other samples, but the number was far fewer and were not regularly-spaced enough to be called a consistent pattern. However, it is clear that since they still occurred along the edges of the visible columnar grains, it is likely that they formed for the same reason as in the other cases, which also exhibited pores only along the edges of the grains present in their material.

These pores could have been caused by one or more of several common mechanisms in SLM. The first is that insufficient energy was supplied by the laser to fully melt the powder at these locations, which in turn prevented the necessary adhesion between grains as the material cooled and shrunk [1]. The dislocation mechanisms within the crystal structure in its semi-melted and therefore more ductile state would cause any local dislocations to coalesce at these points along the grain boundaries, resulting in sizeable pores. At faster laser speeds, these cases of insufficient energy for melting would be more frequent and therefore result in smaller and more regularly ordered pores along these boundaries, whereas at slower speeds, there would be fewer unmelted areas but potentially more cooling time and energy for dislocation motion towards these areas, resulting in more irregular but occasionally larger pores.

Another source of such interruptions in the material could be due to voids left in the wake of the subliming of a secondary-phase material concentration within the metal. Due to the images capture by the SEM, it is clear that some quantity of secondary-phase particles was present throughout the majority of the

samples, and it is known that secondary-phase particles are more likely to form at the grain boundaries than internally. [4] These particles were most likely formed during the sintering process, but due to the combustion temperatures of many of the candidate compounds, it is equally likely that after forming during one pass of the laser over the sample's surface, the next few subsequent passes would have provided sufficient excess energy to then disintegrate them [12]. These would then have left voids behind in the material to become pore nucleation sites.

Once again, the general trend seen in the imaged samples could support this idea. In the slower-speed samples, the longer laser dwell time could have provided more energy for these disintegrating reactions, causing larger pores, while simultaneously providing more time for dislocations to coalesce at these nucleation sites due to longer heating times. The faster speeds, on the other hand, would have less excess energy for this process and a shorter window for pore growth, resulting in smaller but more regular pores.

Since evidence of both unmelted powder and secondary-phase particles were found on almost every tested sample, it is probable that the pores were formed by some combination of the presented possible causes.

$N_2 - H_2$ Sample Pores

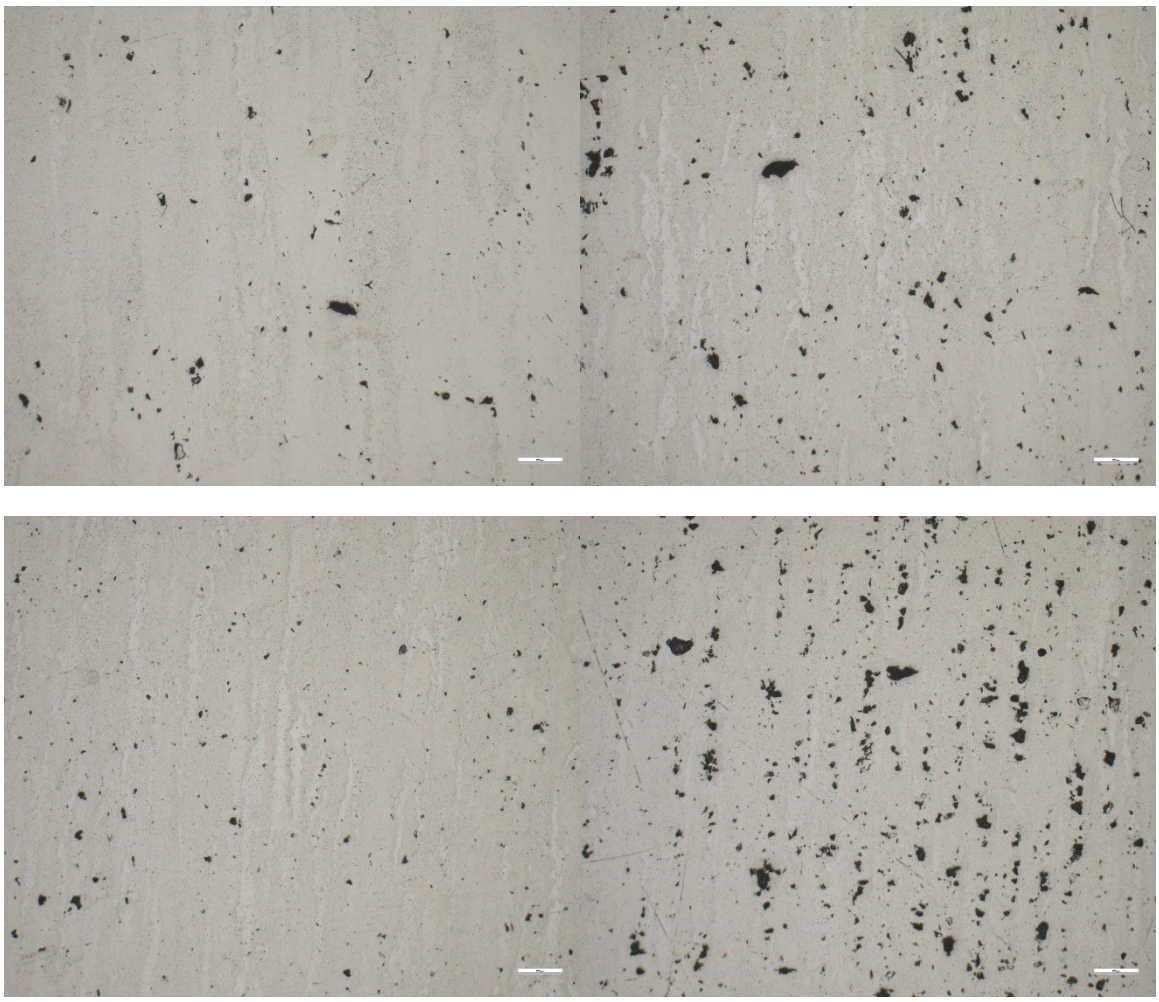

Figure 32. Samples Processed in 2.5% H_2 at 100 mm/s (a), 200 mm/s (b), 400 mm/s (c), and 600 mm/s (d), at 5x Magnification

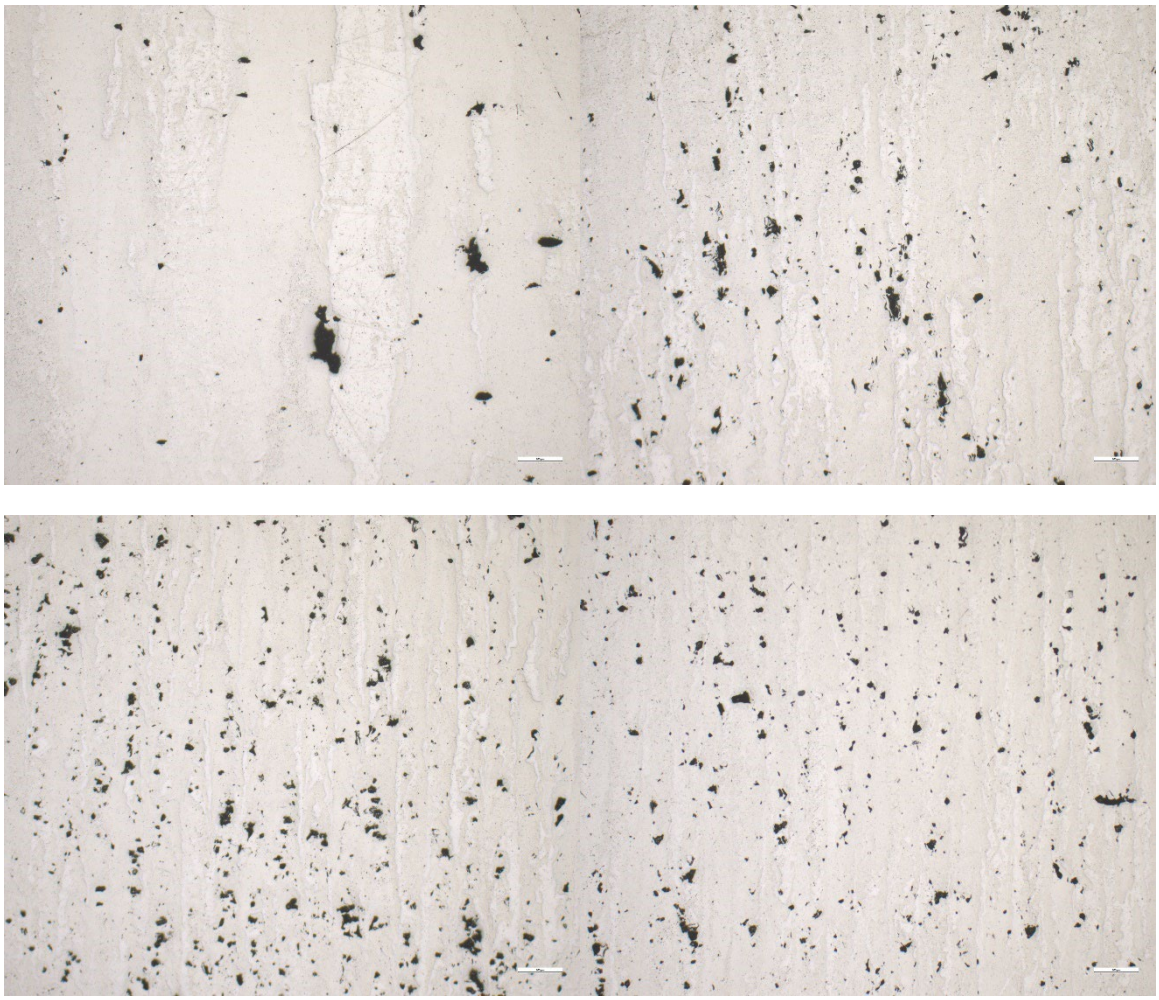

Figure 33. Samples Processed in 5% H_2 at 100 mm/s (a), 200 mm/s (b), 400 mm/s (c), and 600 mm/s (d), at 5x Magnification

The number and size of crack nucleation sites such as these pores is usually closely tied to the overall performance of the material, particularly in applications where vibrational loading is expected. Since the target applications for additively manufactured W include both high-speed aeronautical vehicles and turbine components, performance under vibrational loads is of interest [34]. Therefore, one of the optimization considerations included the number and size of

the pores present in each material sample, with the goal of minimization in each case.

Each image was therefore also processed in a software package that provided data on the number of pores, their dimensions, and total area percentage of the image taken up by these pores.

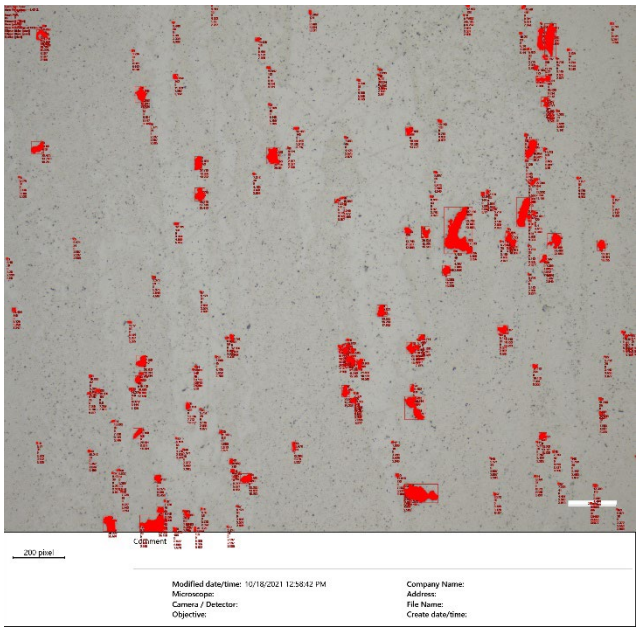

Figure 34. Sample Output Image from Pore Count Image Analysis

Figure 34 shows a representative processed image, and the resulting data sets for each processed image are included in Appendix C. These data sets were collated and averaged, and the general trends in pore number and total area percentage were then plotted in Fig 35 and 36 below. The maximum pore size for each case was also found and recorded, but no significant trends were discernable in the data.

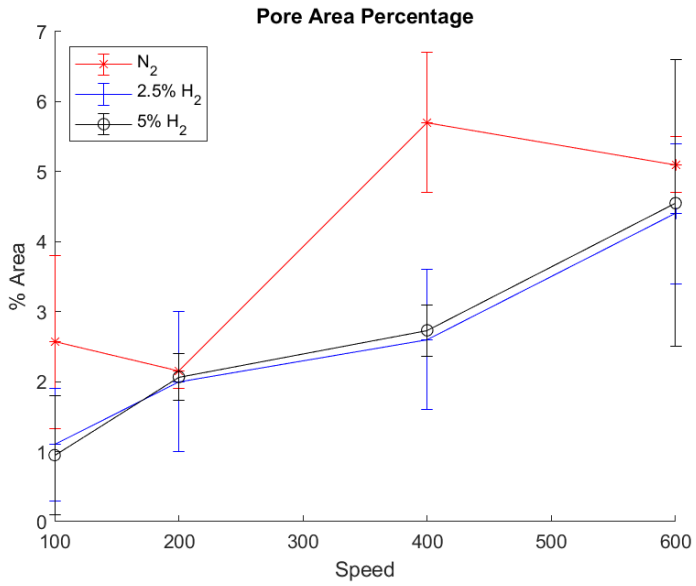

Figure 35. Average Percent Area Containing Pores

Since insufficient unique data points were able to be gathered in order to support an designed experiment ANOVA analysis, averages of the available data points at each speed and for each atmospheric composition were made. The resulting trends are captured in Fig 35 above and show that in general, the percent area of each image containing pores increased with increased scan speed. This result was expected since the energy density drops with speed increase, causing less complete adhesion in the body of the part. However, there was a distinguishable difference between the behavior of the 100% N_2 samples and those processed in atmospheres containing H_2. Those in the N_2 atmosphere appeared to peak in total pore area percentage at 400 mm/s, whereas the others had a steadily rising trend at the edge of the design space.

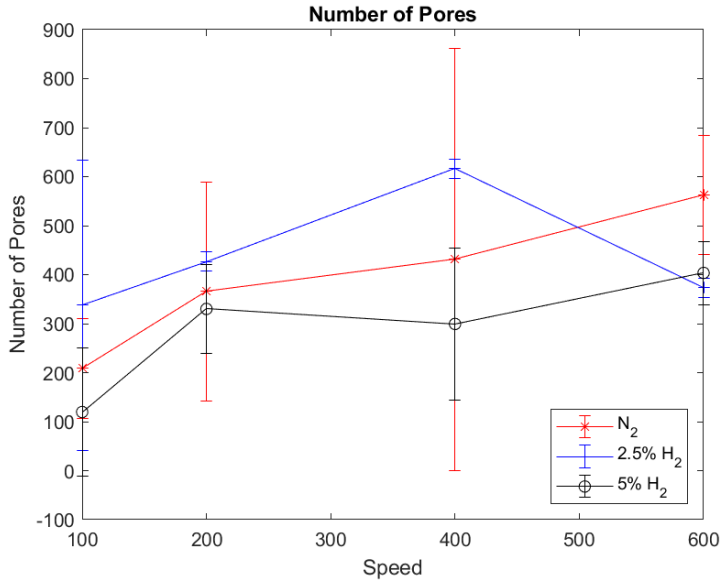

Figure 36. Average Number of Pores

The average number of pores appeared to have relatively little correlation with speed beyond 100 mm/s for the 100% N_2 atmosphere, but there did seen to be a difference between the trends present in the 2.5% H_2 samples and those in the 5% H_2 samples. The 2.5% H_2 trend appeared to have a peak at 400 mm/s, whereas the 5% H_2 trend rose at 200 mm/s and stayed relatively consistent throughout the rest of the design space. The 5% H_2 trend also remained the lowest out of the three atmospheres, which together with the trends from Fig 35 suggest that while these samples contained fewer pores, they were larger on average than those found in the atmospheres with less H_2. This would indicate that increased H_2 in the build atmosphere could have been a driving factor in decreased cohesion between the grains running parallel to the laser's track.

Since in previous studies, lack of grain boundary cohesion has been attributed to the presence of weakening oxides, [6,7] that is a likely candidate for it in this instance, as well. The competing reactions between N_2, O_2, and H_2

occurring close to the surface of the melted W could have caused stray O molecules that would have otherwise been captured in an N_2 bond in the case of the pure 100% N_2 environment to instead be bounced towards the melted W. This would cause boundary films such as those discussed in the previously mentioned study by Hu, et al [1] to prevent grain adhesion during cooling.

Grain Size

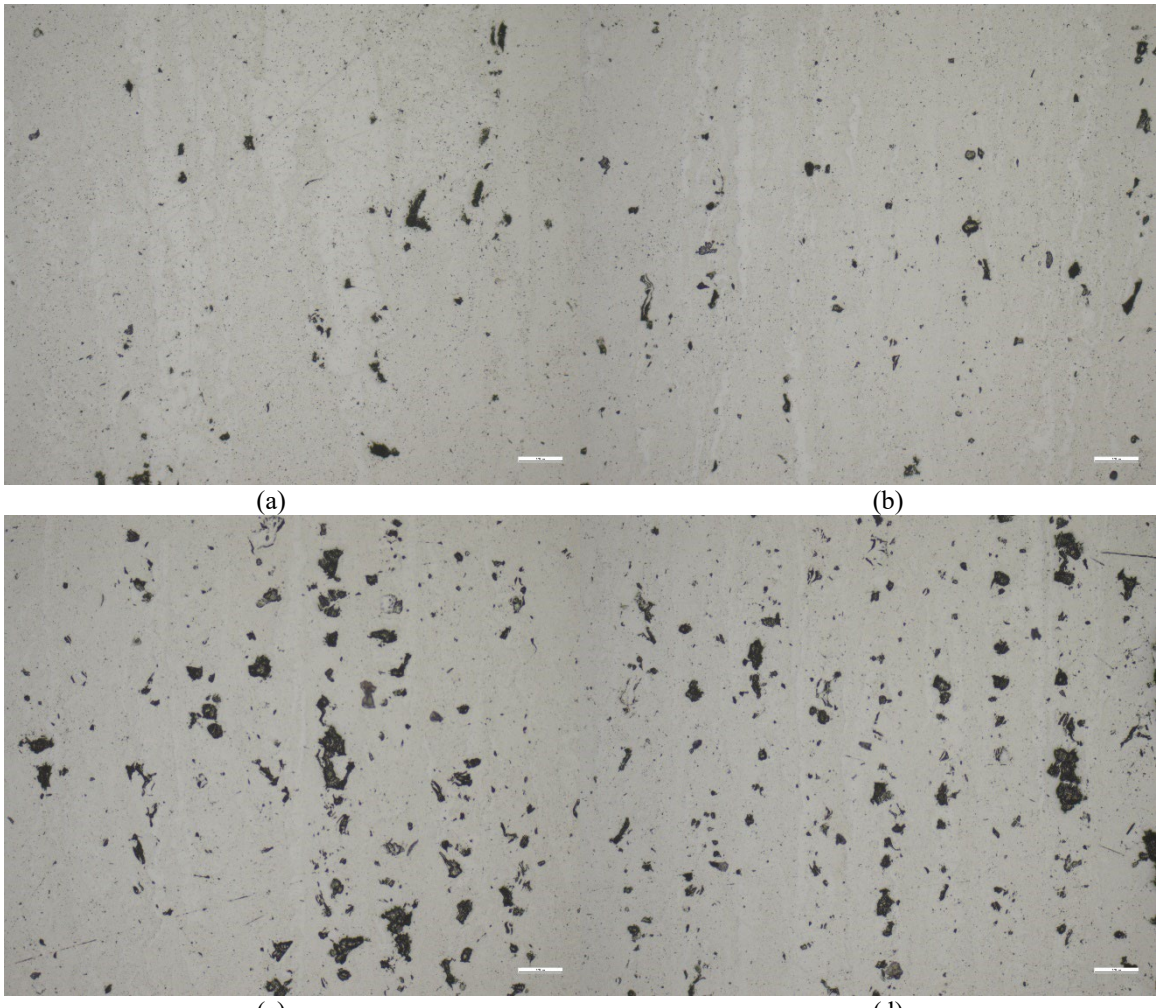

Figure 37. Grains of Samples Processed in 100% N_2 at 100 mm/s (a), 200 mm/s (b), 400 mm/s (c), and 600 mm/s (d)

Another focus of the visible microscopy was examination of relative grain size and general grain characteristics in each sample set. All samples showed signs of elongated grains in the build direction, as shown in Fig 37 above. However, in all cases, the grain widths of the samples processed under the slowest speed exhibited the largest grains by far. The faster speeds, in fact, all had relatively similar grain widths.

These observations appear to align to the typical behavior seen in metals that have undergone heat treatment. Heat treatments usually involve the introduction of enough excess energy to allow the crystals within the metal to preferentially align with each other, which frequently results in larger grains [35]. Therefore, the presence of these much larger grains in the 100 mm/s cases could indicate that the amount of energy supplied by the laser is significantly more than what is required to melt the metal. That energy could instead be being used to orient the metallic crystals into alignment with each other, resulting in much wider grains.

The presence of pores could also have obstructed the growth of larger grains in the faster speeds. In order to align and adhere to its neighbors' orientation, a crystal must be in close proximity to them [29]. Pores would prevent their bordering crystals from achieving this.

Another notable feature of these grains is the undulation of their boundaries. This characteristic can most clearly be seen on the faster speeds and cause the grains to have an almost wispy appearance. It is conjectured that this is due to the influence of gravity on the melted W during sintering. This behavior

has previously been observed in W [1] and is credited to the molten metal pooling over the course of several passes, which allows for motion perpendicular to the build direction and irregular, oxbow shapes to form as the metal flows down the path of least resistance and in accordance with gravity.

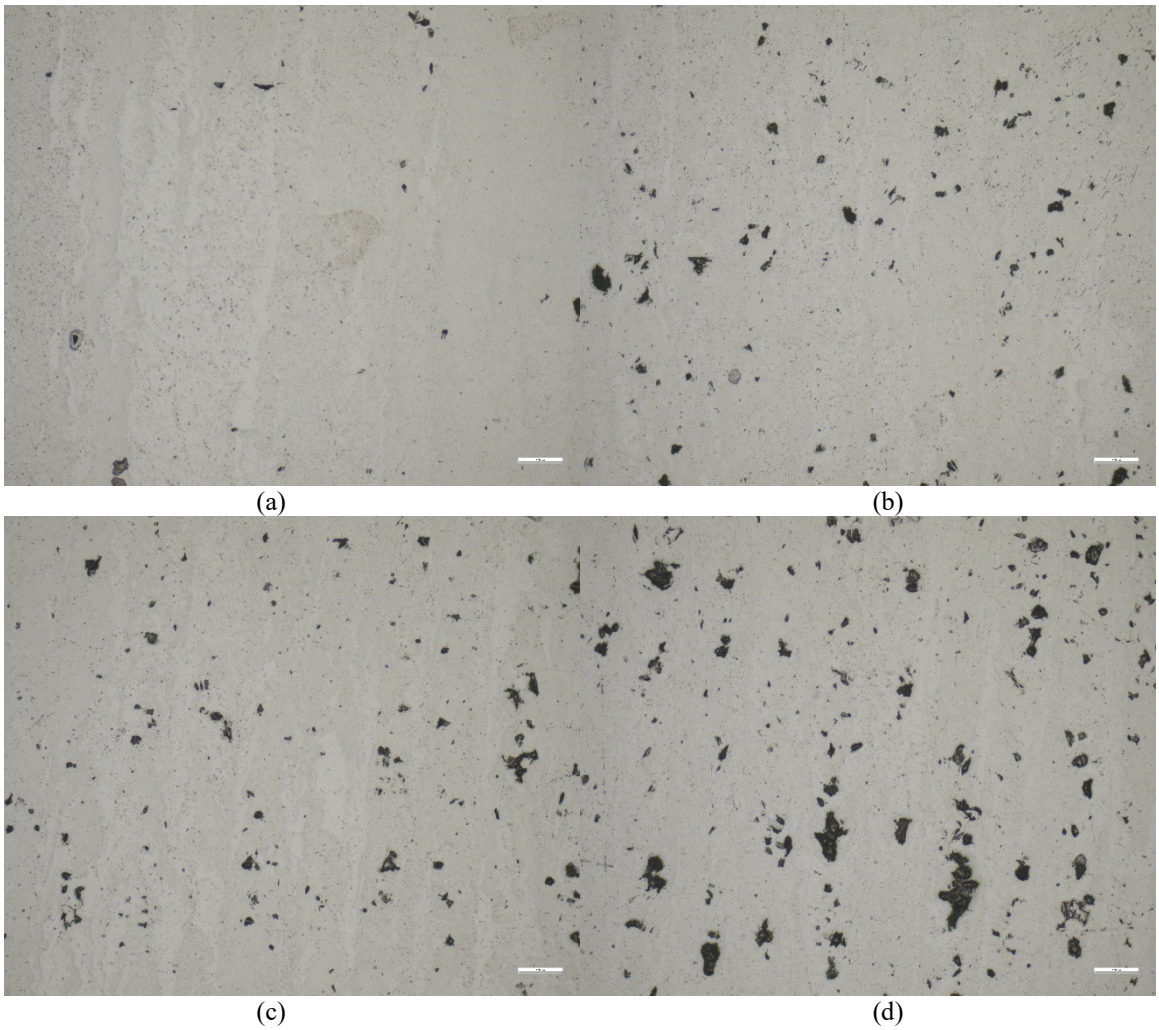

Figure 38. Grains of Samples Processed in 2.5% H_2 at 100 mm/s (a), 200 mm/s (b), 400 mm/s (c), and 600 mm/s (d)

In both set of samples that had H_2 present in their build chambers, there seemed to be a slight decrease in the number of pores per image, but the pores that were present often appeared larger, and in some cases looked as if they could

be results of smaller, more closely-spaced pores connecting prior to cooling. The visible grains appeared similar to those from the 100% N_2 builds, but they appeared to grow progressively larger with the addition of more H_2, as can be seen in Fig 38 and 39.

Whereas H_2 in the build environment proved beneficial in shrinking grain size and strengthening grain boundaries in an otherwise inert atmosphere like Ar,[7] in this case, it resulted in larger grains. Since in W, impurities are known to collect at the grain boundaries and weaken them[4,6,7], the images collected from this experiment support the previous conclusion that adding H_2 to an N_2-dominant environment would not be likely to increase part strength.

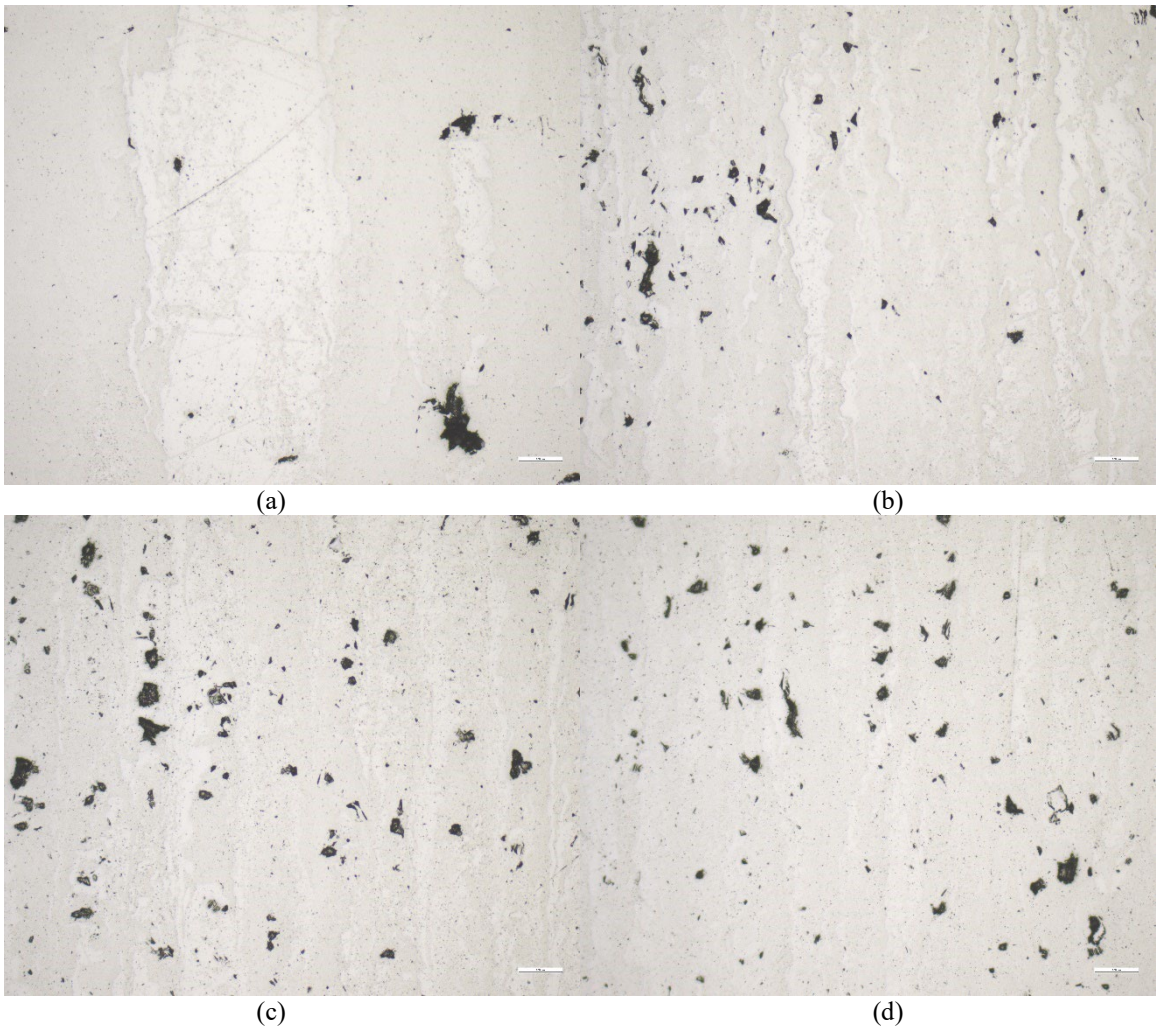

Figure 39. Grains of Samples Processed in 5% H_2 at 100 mm/s (a), 200 mm/s (b), 400 mm/s (c), and 600 mm/s (d), at 5x Magnification

Hardness Test Analysis

Table 7. Hardness Test Results (HV1)

Laser Speed (mm/s)	100	200	400	600
100% N_2	361.47	318.22	314.36	306.80
2.5% H_2	324.73	331.91	353.91	326.33
5% H_2	340.12	316.78	318.33	310.40

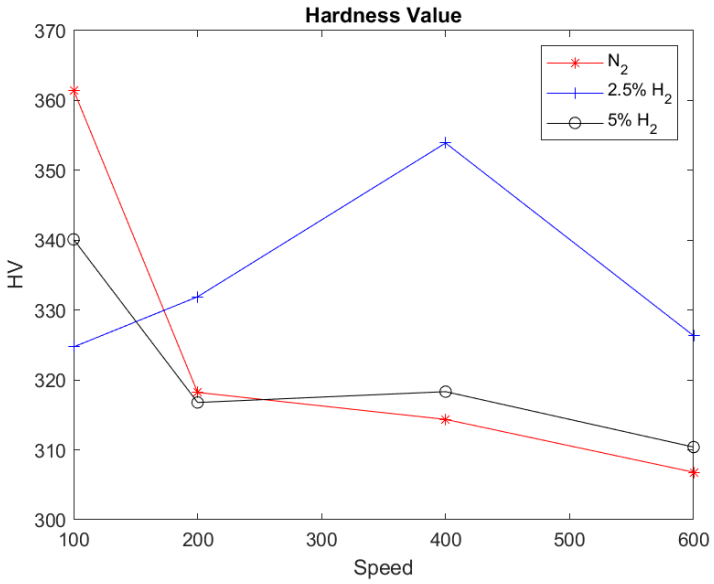

Figure 40. Hardness Values from Atmospheric Variance Experiment

The trends in hardness value are plotted in Fig 40 above. All values are close to the expected minimum hardness for traditionally manufactured W, which typically has a range of 300-650 HV30. This is borne out in the results from the three-point bend tests, which also exhibited maximum stress values that were low to average when compared to the results of other studies [6,7]. However, the difference in shape between the 2.5% H_2 curve and the other two curves indicate possible curvature in the hardness value response surface. While the highest average value is from the 100 mm/s specimens built in 100% N_2, this does not correspond to the parameters for the highest-strength samples. There have also been other disadvantages to printing at the slowest speed that have previously been discussed, including largest grain size, largest cracks, and lowest ductility. Therefore, if greater hardness is desired, there would be value in shifting the peak of the hardness value curve to the right, which the 2.5% H_2case appears to do.

Summary

The results of the designed experiment regarding the effects of an $N_2 - H_2$ atmosphere on additively manufactured pure W were presented and analyzed. The chemical composition data showed promising reductions in O relative to previous experimentation, while the hardness data revealed that all print conditions resulted in relatively soft yet brittle W. The optical microscopy and SEM images showed relatively porous, large-grained, and cracked surfaces with evidence of sputtering but little oxidation that could be attributed to the build process. The oxides that did form during high-temperature testing appeared to be WO_3, which is known to sublime at higher temperatures. However, the ANOVA models for material strength and ductility proved that it was possible to achieve properties similar in strength to traditionally manufactured W when processed in the pure N_2 atmosphere.

V. Conclusions and Recommendations

Conclusions of Research

The results of this experiment showed both strengths and weaknesses in the chosen manufacturing process. The chemical composition data indicated that the O content and therefore the oxide content of the specimens was significantly reduced relative to the $Ar - H_2$ study [7]. However, the ANOVA models showed that the lower levels of oxidation did not result in stronger W than that recorded in the previous study. This was hypothesized to have happened because the interstitial oxide strengthening mechanisms postulated in the $Ar - H_2$ study were unable to form in the melted W due to the far more reactive $N_2 - H_2$ environment.

The ANOVA models showed that it was possible to achieve W specimens with comparable strength properties to hot-rolled W, but the combination of N_2 and H_2 proved counterproductive. While the $Ar - H_2$ study [7] had indicated that the addition of the H_2 should result in stronger, less brittle W with fewer cracks and pores, it is conjectured that the atmosphere was made more unstable in this case because the H_2 was added to an already chemically reactive environment of N_2. The different formation and dissociation rates of these two gases with O may have caused uneven energy distribution within the melting W, resulting in stress concentrations, and the dissociated O could also have formed oxide films on the surface of the melt pool, which could have sublimated, absorbing energy from the laser needed for appropriate weld adhesion.

One unexpected but interesting trend from the models was that there was a small increase in strength with increased scan speed, which is typically not the case. This could aid in reducing part lead time, which is beneficial for rapid prototyping. The likely reason for this strength increase was exhibited in the SEM imagery, which showed that the slow-speed samples consisted of large, columnar structures with large cracks along their boundaries, whereas the faster laser speeds produced samples with more irregular crack patterns and smaller, more close-packed grains.

The SEM images also showed increased sputtering in the samples built in an $N_2 - H_2$ atmosphere. This lends credence to the idea that uneven energy was being introduced into the melted W, which in turn resulted in stress concentrations leading to increased cracking and reduced strength and ductility. Since the imagery showed so little oxidation, this is proposed to be the main weakening mechanism in this build process.

The optical microscopy also showed evidence of the large grains shown in the SEM imagery, along with a significant number of pores in all samples. However, smaller pores and grains were seen in the samples processed in faster laser speeds, which aligned with the theories proposed regarding the link between increased material strength and laser speed.

The hardness data showed that all the samples were soft and brittle compared to traditionally manufactured W. However, the trends within the data showed that the pure N_2 environment produced the hardest samples, albeit at the slowest laser speed. Since the faster laser speed samples proved to be significantly stronger than the slower ones in the ANOVA models, it may be preferable to seek peak material strength rather than peak hardness, but if both are required, the hardness data showed that higher hardness at faster laser speeds could be achieved if 2.5% H_2 was added to the build atmosphere.

Since very little previous study was subject to ANOVA or any other optimization method, there are some limitations in the accuracy of comparisons between the data from this experiment and that in other bodies of work. Confidence values were not reported for the majority of papers, and the numbers of samples tested in their experiments were relatively low for undesigned experiments. This could introduce large margins of error in their quantitative data that were not explicitly expressed. Therefore, while the confidence that the data resulting from the designed experiment represents the trends and value ranges present in the global population of samples produced under the exact conditions of its particular build process is high, the accuracy of any comparisons between this data and that from other research is less reliable.

Furthermore, not all of the quantitative data was able to be subjected to ANOVA analysis. Oversights on the part of the test conductor resulted in only one replication of hardness and pore analyzation data to be collected, which resulted in much lower confidence for these two analyses.

Recommendations for Future Research

Several avenues of further experimentation were illuminated during this experiment. Foremost, it is recommended that future research expand the scope of the laser speed factor to determine the extent to which further increases in laser speed might benefit the material strength. Similarly, expanding the temperature test range to examine its effect on the oxidation and reduction cycle of W -and by extension its compositional integrity and strength- would greatly benefit future application research.

Experimentation to verify the validity of the proposed mechanism of strength reduction in the $N_2 - H_2$ build atmosphere has also been suggested by Major Ryan Kemnitz [36]. The relative temperature variations experienced by samples built in atmospheric air, N_2, Ar, $N_2 - H_2$, and $Ar - H_2$ build environments could be compared to determine the differences in heat energy experienced in each case, which could indicate the extent to which the strength of these materials is impacted by these fluctuations.

It is also recommended that other traditional methods of improving metal strength and ductility be explored in a designed experiment, such as heat treatment, dopants, and alloying, since these avenues have yet to be explored.

Summary

This experiment has demonstrated the strengths and weaknesses of the additive manufacturing process in an $N_2 - H_2$ build environment for W by subjecting samples of W built under these conditions to a designed mechanical testing experiment supplemented by qualitative analyses. This provides a platform for easy augmentation of the existing design as well as a template and basis for future research efforts on W and proves the capability of the subject build process to produce material with comparable properties to that of traditionally manufactured metal.

Appendix A

```
% cd points Matlab to the folder with the data folders
cd 'C:\Users\dionn\Documents\Thesis\Room Temp N2'
B = dir('**/*.txt');

% Time to step through all the text files and extract the data
for i = 1:length(B);
    file = [B(i).folder,'\',B(i).name];
    temp = importdata(file);


    % the data is compressive, so this makes everything positive for ease
    % of visualization
    A{i} = -temp.data;

    % sometimes you aren't in good contact until you experience a tiny bit
    % of force, this next bit just detects where loading really begins
    first_loc = find(A{i}(:,2)>2e-3,1);
    A{i}(:,1) = A{i}(:,1)-A{i}(first_loc,1);

    % often times, the end of the data happened around 0.5 mm, so I set
    % this bit to cut off the SLAM at the end of the test, YMMV on whether
    % this value is useful or good
    last_loc = find(A{i}(:,1)>0.5,1);
    if isempty(last_loc) == true
        last_loc = length(A{i}(:,1));
    end

    % FINALLY, cut off the early and late bits of the data and save the
    % data you want to keep as C
    C{i} = A{i}(first_loc:last_loc-3,:);

    % optional plotting to see if your data files make sense
%      hold on
%      plot(C{i}(:,1),C{i}(:,2))

    % store the max load (N) as val, and the displacement at max load as
    % max_disp, so simple
     [val(i,1),loc] = max(C{i}(:,2));
    max_disp(i,1) = C{i}(loc,1);
    brstress(i,1)=C{i}(end,2);
    brstrain(i,1)=C{i}(end,1);
end

% put in the speeds for which you have valid tests here
% I tried to pre-format speeds for you data
speeds = [100;100;100;200;200;200;400;400;400;600;600;600];
unique_speeds = unique(speeds);

clear M
% put in your measurements data file in the same directory!
% the next few lines try to make sense of the measurements for calculating
% stress
M = importdata('W-N2 Sample Measurements.xlsx');
dims = M.data;

dims(:,1) = [];
dims(1,:) = [];
```

```
widths = dims(:,2);
thicks = dims(:,3);

% All the data is in, time to calculate stress and take averages

real_stress = 3*val*1000*14./(2*widths.*thicks.^2);
real_strain = 6*max_disp.*thicks/14^2;
break_stress = 3*brstress*1000*14./(2*widths.*thicks.^2);
break_strain = 6*brstrain.*thicks/14^2;

for i = 1:length(unique_speeds)
    o = (i-1)*3+1;
    p = i*3;
    locs = find(speeds==unique_speeds(i))
    average_stress(i) = mean(real_stress(locs));
    average_strain(i,1) =100*mean(real_strain(locs));
    stress_err(i,1) = std(real_stress(locs));
    strain_err(i,1) = 100*std(real_strain(locs));

end

EV = 200./(0.020*0.050*unique_speeds);


% I recommend renaming this bit at the end of each code snippet to
% something describing the data like... W_N2, W_2_H2, W_5_H2, etc...
% each snippet of code uses more or less the same variables, so do a...
% clearvars -except W_N2 W_2_H2 W_5_H2, to only save those bits
W_N2 = [unique_speeds EV average_stress' average_strain stress_err strain_err];
W_N2_real = [real_stress real_strain break_stress break_strain];
clearvars -except W_N2 W_N2_real W_N2_2H2 W_N2_5H2

% cd points Matlab to the folder with the data folders
cd 'C:\Users\dionn\Documents\Thesis\Room Temp N2-2.5H2'
B = dir('**/*.txt');

% Time to step through all the text files and extract the data
for i = 1:length(B);
    file = [B(i).folder,'\',B(i).name];
    temp = importdata(file);


    % the data is compressive, so this makes everything positive for ease
    % of visualization
    A{i} = -temp.data;

    % sometimes you aren't in good contact until you experience a tiny bit
    % of force, this next bit just detects where loading really begins
    first_loc = find(A{i}(:,2)>2e-3,1);
    A{i}(:,1) = A{i}(:,1)-A{i}(first_loc,1);

    % often times, the end of the data happened around 0.5 mm, so I set
    % this bit to cut off the SLAM at the end of the test, YMMV on whether
    % this value is useful or good
    last_loc = find(A{i}(:,1)>0.5,1);
    if isempty(last_loc) == true
        last_loc = length(A{i}(:,1));
    end
```

```
    % FINALLY, cut off the early and late bits of the data and save the
    % data you want to keep as C
    C{i} = A{i}(first_loc:last_loc-3,:);

    % optional plotting to see if your data files make sense
%       hold on
%       plot(C{i}(:,1),C{i}(:,2))

    % store the max load (N) as val, and the displacement at max load as
    % max_disp, so simple
     [val(i,1),loc] = max(C{i}(:,2));
    max_disp(i,1) = C{i}(loc,1);
        brstress(i,1)=C{i}(end,2);
    brstrain(i,1)=C{i}(end,1);
end

% put in the speeds for which you have valid tests here
% I tried to pre-format speeds for you data
speeds = [100;100;100;200;200;200;400;400;400;600;600;600];
unique_speeds = unique(speeds);

clear M
% put in your measurements data file in the same directory!
% the next few lines try to make sense of the measurements for calculating
% stress
M = importdata('W-N2-2.5H2 Sample Measurements.xlsx');
dims = M.data;

dims(:,1) = [];
dims(1,:) = [];

widths = dims(:,2);
thicks = dims(:,3);

% All the data is in, time to calculate stress and take averages

real_stress = 3*val*1000*14./(2*widths.*thicks.^2);
real_strain = 6*max_disp.*thicks/14^2;
break_stress = 3*brstress*1000*14./(2*widths.*thicks.^2);
break_strain = 6*brstrain.*thicks/14^2;

for i = 1:length(unique_speeds)
    o = (i-1)*3+1;
    p = i*3;
    locs = find(speeds==unique_speeds(i))
    average_stress(i) = mean(real_stress(locs));
    average_strain(i,1) =100*mean(real_strain(locs));
    stress_err(i,1) = std(real_stress(locs));
    strain_err(i,1) = 100*std(real_strain(locs));

end

EV = 200./(0.020*0.050*unique_speeds);


% I recommend renaming this bit at the end of each code snippet to
% something describing the data like... W_N2, W_2_H2, W_5_H2, etc...
% each snippet of code uses more or less the same variables, so do a...
```

```
% clearvars -except W_N2 W_2_H2 W_5_H2, to only save those bits
W_N2_2H2 = [unique_speeds EV average_stress' average_strain stress_err strain_err];
W_N2_2H2_real = [real_stress real_strain break_stress break_strain];
clearvars -except W_N2 W_N2_real W_N2_2H2 W_N2_2H2_real W_N2_5H2

% cd points Matlab to the folder with the data folders
cd 'C:\Users\dionn\Documents\Thesis\Room Temp N2-5H2'
B = dir('**/*.txt');

% Time to step through all the text files and extract the data
for i = 1:length(B);
    file = [B(i).folder,'\',B(i).name];
    temp = importdata(file);


    % the data is compressive, so this makes everything positive for ease
    % of visualization
    A{i} = -temp.data;

    % sometimes you aren't in good contact until you experience a tiny bit
    % of force, this next bit just detects where loading really begins
    first_loc = find(A{i}(:,2)>2e-3,1);
    A{i}(:,1) = A{i}(:,1)-A{i}(first_loc,1);

    % often times, the end of the data happened around 0.5 mm, so I set
    % this bit to cut off the SLAM at the end of the test, YMMV on whether
    % this value is useful or good
    last_loc = find(A{i}(:,1)>0.5,1);
    if isempty(last_loc) == true
        last_loc = length(A{i}(:,1));
    end

    % FINALLY, cut off the early and late bits of the data and save the
    % data you want to keep as C
    C{i} = A{i}(first_loc:last_loc-3,:);

    % optional plotting to see if your data files make sense
%      hold on
%      plot(C{i}(:,1),C{i}(:,2))

    % store the max load (N) as val, and the displacement at max load as
    % max_disp, so simple
     [val(i,1),loc] = max(C{i}(:,2));
    max_disp(i,1) = C{i}(loc,1);
        brstress(i,1)=C{i}(end,2);
    brstrain(i,1)=C{i}(end,1);
end

% put in the speeds for which you have valid tests here
% I tried to pre-format speeds for you data
speeds = [100;100;100;200;200;200;400;400;400;600;600;600];
unique_speeds = unique(speeds);

clear M
% put in your measurements data file in the same directory!
% the next few lines try to make sense of the measurements for calculating
% stress
M = importdata('W-N2-5H2 Sample Measurements.xlsx');
dims = M.data;
```

```
dims(:,1) = [];
dims(1,:) = [];

widths = dims(:,2);
thicks = dims(:,3);

% All the data is in, time to calculate stress and take averages

real_stress = 3*val*1000*14./(2*widths.*thicks.^2);
real_strain = 6*max_disp.*thicks/14^2;
break_stress = 3*brstress*1000*14./(2*widths.*thicks.^2);
break_strain = 6*brstrain.*thicks/14^2;

for i = 1:length(unique_speeds)
    o = (i-1)*3+1;
    p = i*3;
    locs = find(speeds==unique_speeds(i))
    average_stress(i) = mean(real_stress(locs));
    average_strain(i,1) =100*mean(real_strain(locs));
    stress_err(i,1) = std(real_stress(locs));
    strain_err(i,1) = 100*std(real_strain(locs));

end

EV = 200./(0.020*0.050*unique_speeds);


W_N2_5H2 = [unique_speeds EV average_stress' average_strain stress_err strain_err];
W_N2_5H2_real = [real_stress real_strain break_stress break_strain];
hold on
errorbar(W_N2(:,1),W_N2(:,3),W_N2(:,5),'-b+')
errorbar(W_N2_2H2(:,1),W_N2_2H2(:,3),W_N2_2H2(:,5),'-r*')
errorbar(W_N2_5H2(:,1),W_N2_5H2(:,3),W_N2_5H2(:,5),'-ko')
title 'Stress vs Scan Speed'
xlabel 'Scan Speed (mm/s)'
ylabel 'Stress (MPa)'
legend('W,N_2, 600C','W,N_2-2.5H_2, 600C','W,N_2-5H_2, 600C','W,N_2','W,N_2-

2.5H_2','W,N_2-5H_2')
```

Appendix B

```
%% W, N2

clear all
close all
clc

cd 'C:\Users\dionn\Documents\Thesis\600C N2'
B = dir('**/*.txt'); %read files


for i = 1:length(B)
    file = [B(i).folder,'\',B(i).name];
%     temp = importdata(file,'HeaderLines',3);
    temp = readtable(file,'HeaderLines',3);
    if size(temp,2) > 3
        temp(:,4:size(temp,2)) = [];
    end

    temp = table2array(temp);
    A{i} = -temp;

    last_loc = find(A{i}(:,2)>0.5,1);
    if isempty(last_loc) == true
        last_loc = length(A{i}(:,2));
    end

    C{i} = A{i}(1:last_loc-3,:);


     [val(i,1),loc] = max(C{i}(:,3));
     dp(i,1) = C{i}(loc,2);
     brstress(i,1)=C{i}(end,3);
     brstrain(i,1)=C{i}(end,2);
end %make forces positive and get max force + corresponding displacement

clear M
% put in your measurements data file in the same directory!
% the next few lines try to make sense of the measurements for calculating
% stress
M = importdata('W_N2_600C.xlsx');
dims = M.data;

widths = dims(:,1);
thicks = dims(:,2);

angle = atand(dp/7); %get bend angle (degrees)
stress = 3*val*14./(2*widths.*thicks.^2); %get true stress (MPa)
strain = 6*dp.*thicks/14^2;
break_stress = 3*brstress*14./(2*widths.*thicks.^2);
break_strain = 6*brstrain.*thicks/14^2;

speeds = [100;100;100;200;200;200;400;400;400;600;600;600];
unique_speeds = unique(speeds);

for i = 1:length(unique_speeds)
    locs = find(speeds==unique_speeds(i));
```

```
    avgstress(i) = mean(stress(locs));
    avgangle(i) = mean(angle(locs));
    stress_err(i,1) = std(stress(locs));
end

errorbar(unique_speeds,avgstress,stress_err,'s','Linewidth',2) %plot stress v speeds
for each temp
title 'Stress vs Scan Speed'
xlabel 'Scan Speed (mm/s)'
ylabel 'Stress (MPa)'
legend('W,N_2', 'W,N_2-2.5H_2','W,N_2-5H_2')
hold on
%
% j=1; k=0;
% for i = 1:Params*length(unique_speeds)
%     locs = find(speeds==unique_speeds(j));
%     avgstress(j) = mean(stress(locs+k*Tests));
%     avgangle(j) = mean(angle(locs+k*Tests));
%     j = j+1;
%
%     if mod(i,4) == 0
%         plot(unique_speeds,avgstress,'s','Linewidth',2) %plot stress v speeds for
each temp
%         title 'Stress vs Scan Speed'
%         xlabel 'Scan Speed (mm/s)'
%         ylabel 'Stress (MPa)'
%         legend('W-0.1HfC, H2','W,Ar','W,H2')
%         hold on
%
% %         figure
% %         plot(unique_speeds,avgstress,'s','Linewidth',2) %%plot bend angle v speeds
% %         title 'Bend Angle vs Scan Speed'
% %         xlabel 'Scan Speed (mm/s)'
% %         ylabel 'Bend Angle (degrees)'
% %         legend('W-0.1HfC, H2','W,Ar','W,H2')
% %         hold on
%
%         j = 1;
%         k = k+1;
%     end
% end

WN2 = [unique_speeds avgangle' avgstress' stress_err];
WN2real = [stress strain break_stress break_strain];
%% W N2-2.5H2

cd 'C:\Users\dionn\Documents\Thesis\600C N2-2.5H2'
B = dir('**/*.txt'); %read files


for i = 1:length(B)
    file = [B(i).folder,'\',B(i).name];
    %temp = importdata(file,'HeaderLines',6);
    temp = readtable(file,'HeaderLines',3);
    if size(temp,2) > 3
        temp(:,4:size(temp,2)) = [];
    end

    temp = table2array(temp);
```

```
    A{i} = -temp;

    last_loc = find(A{i}(:,2)>0.5,1);
    if isempty(last_loc) == true
        last_loc = length(A{i}(:,2));
    end

    C{i} = A{i}(1:last_loc-3,:);

     [val(i,1),loc] = max(C{i}(:,3));
     dp(i,1) = C{i}(loc,2);
     brstress(i,1)=C{i}(end,3);
     brstrain(i,1)=C{i}(end,2);
end %make forces positive and get max force + corresponding displacement

clear M
% put in your measurements data file in the same directory!
% the next few lines try to make sense of the measurements for calculating
% stress
M = importdata('W_2H2_600C.xlsx');
dims = M.data;

widths = dims(:,1);
thicks = dims(:,2);

angle = atand(dp/7); %get bend angle (degrees)
stress = 3*val*14./(2*widths.*thicks.^2); %get true stress (MPa)
strain = 6*dp.*thicks/14^2;
break_stress = 3*brstress*14./(2*widths.*thicks.^2);
break_strain = 6*brstrain.*thicks/14^2;

speeds = [100;100;100;200;200;200;400;400;400;600;600;600];
unique_speeds = unique(speeds);

for i = 1:length(unique_speeds)
    locs = find(speeds==unique_speeds(i));

    avgstress(i) = mean(stress(locs));
    avgangle(i) = mean(angle(locs));
    stress_err(i,1) = std(stress(locs));
end

errorbar(unique_speeds,avgstress,stress_err,'s','Linewidth',4) %plot stress v speeds
for each temp
title 'Stress vs Scan Speed'
xlabel 'Scan Speed (mm/s)'
ylabel 'Stress (MPa)'
legend('W,N_2', 'W,N_2-2.5H_2','W,N_2-5H_2')

WN22H2 = [unique_speeds avgangle' avgstress' stress_err];
WN22H2real = [stress strain break_stress break_strain];
%% W, 5H2

cd 'C:\Users\dionn\Documents\Thesis\600C N2-5H2'
B = dir('**/*.txt'); %read files


for i = 1:length(B)
    file = [B(i).folder,'\',B(i).name];
```

```
    %temp = importdata(file,'HeaderLines',6);
    temp = readtable(file,'HeaderLines',3);
    if size(temp,2) > 3
        temp(:,4:size(temp,2)) = [];
    end

    temp = table2array(temp);
    A{i} = -temp;

    last_loc = find(A{i}(:,2)>0.5,1);
    if isempty(last_loc) == true
        last_loc = length(A{i}(:,2));
    end

    C{i} = A{i}(1:last_loc-3,:);

     [val(i,1),loc] = max(C{i}(:,3));
     dp(i,1) = C{i}(loc,2);
     brstress(i,1)=C{i}(end,3);
     brstrain(i,1)=C{i}(end,2);
end %make forces positive and get max force + corresponding displacement

clear M
% put in your measurements data file in the same directory!
% the next few lines try to make sense of the measurements for calculating
% stress
M = importdata('W_5H2_600C.xlsx');
dims = M.data;

widths = dims(:,1);
thicks = dims(:,2);

angle = atand(dp/7); %get bend angle (degrees)
stress = 3*val*14./(2*widths.*thicks.^2); %get true stress (MPa)
strain = 6*dp.*thicks/14^2;
break_stress = 3*brstress*14./(2*widths.*thicks.^2);
break_strain = 6*brstrain.*thicks/14^2;

speeds = [100;100;100;200;200;200;400;400;400;600;600;600];
unique_speeds = unique(speeds);

for i = 1:length(unique_speeds)
    locs = find(speeds==unique_speeds(i));

    avgstress(i) = mean(stress(locs));
    avgangle(i) = mean(angle(locs));
    stress_err(i,1) = std(stress(locs));
end

WN25H2 = [unique_speeds avgangle' avgstress' stress_err];
WN25H2real = [stress strain break_stress break_strain];
errorbar(unique_speeds,avgstress,stress_err,'s','Linewidth',2) %plot stress v speeds
for each temp
title 'Stress vs Scan Speed'
xlabel 'Scan Speed (mm/s)'
ylabel 'Stress (MPa)'
legend('W,N_2, 600C', 'W,N_2-2.5H_2, 600C','W,N_2-5H_2, 600C')
```

Appendix C

N2	% Area	Number	Max Pore Area (µm^2)
100	1.4	177	2255
100	3.8	139	15822.5
100	2.5	311	11757
200	1.9	142	7844.5
200	2.4	589	1801.25
400	5.7	431	5096.75
600	5.5	684	2813.25
600	4.7	442	6230
2.5H2	%	Number	Max Pore Area (µm^2)
100	1.9	633	5454.25
100	0.3	42	808.25
200	2	427	1884.25
400	2.6	616	2369.25
600	4.4	373	6445.75
5H2	%	Number	Max Pore Area (µm^2)
100	0.2	121	204
100	0.6	65	1655.75
100	0.9	68	7521.75
100	1.8	111	17524
100	1.3	250	2171.25
100	0.9	103	6569.5
200	2.4	310	3014.25
200	1.6	259	2873.25
200	2.2	421	1834.75
400	3	245	2646.5
400	3.1	454	2768.75
400	2.1	199	4601.25
600	6.6	468	6280.75
600	2.5	339	2277.75

References

[1] Hu, Z., Zhao, Y., Guan, K., Wang, Z., and Ma, Z., "Pure tungsten and oxide dispersion strengthened tungsten manufactured by selective laser melting: Microstructure and cracking mechanism," *Additive Manufacturing*, vol. 36, Sep. 2020, pp. 1–11.

[2] Ghosh, S. K., Das, A. K., and Saha, P., "Selective Laser Sintering: A case study of tungsten carbide and Cobalt Powder Sintering by pulsed nd:YAG laser," *Lasers Based Manufacturing*, 2015, pp. 441–459.

[3] TotalMateria, "Refractory metals: Tungsten and tungsten alloys," *Refractory Metals: Tungsten and Tungsten alloys :: Total Materia Article* Available: https://www.totalmateria.com/page.aspx?ID=CheckArticle&site=ktn&NM=110.

[4] Lassner, E., and Schubert, W.-D., *Tungsten: Properties, chemistry, technology of the element, alloys, and chemical compounds*, New York, Boston, Dordrecht, L, : Plenum Publishers, 2013.

[5] MatWeb, *Tungsten, W* Available: http://www.matweb.com/search/DataSheet.aspx?MatGUID=41e0851d2f3c417ba69ea0188fa570e3.

[6] Eckley, C. C., Kemnitz, R. A., Fassio, C. P., Hartsfield, C. R., and Leonhardt, T. A., "Selective laser melting of tungsten-rhenium alloys," *JOM*, vol. 73, Jun. 2021, pp. 3439–3450.

[7] Kemnitz, R. A., Eckley, C. C., Sexton, B. M., and LeSieur, A. R., *Strengthening of additively manufactured tungsten by use of hydrogen in argon shielding gas*, 2022.

[8] Baker, S., and Rogers, N., Cornell University, 2019.

[9] Simchi, A., "Direct laser sintering of metal powders: Mechanism, kinetics and microstructural features," *Materials Science and Engineering: A*, vol. 428, Apr. 2006, pp. 148–158.

[10] Dong, J., Liu, S., Chen, H., Li, D., Zhang, T., Chen, C., and Zhou, K., "Effect of atmosphere on the microstructure and properties of additively manufactured tungsten," *Materials Science and Technology*, vol. 36, Nov. 2020, pp. 1988–1996.

[11] NIST, *Nitric oxide* Available: https://webbook.nist.gov/cgi/cbook.cgi?ID=C10102439&Mask=1.

[12] NIST, "Tungsten trioxide," *tungsten trioxide* Available: https://webbook.nist.gov/cgi/cbook.cgi?ID=C1314358&Units=SI&Mask=2.

[13] NIST, *Water* Available: https://webbook.nist.gov/cgi/cbook.cgi?ID=C7732185&Mask=2.

[14] Venables, D. S., and Brown, M. E., "Reduction of tungsten oxides with hydrogen and with hydrogen and carbon," *Thermochimica Acta*, vol. 285, Feb. 1996, pp. 361–382.

[15] Vrancken, B., King, W. E., and Matthews, M. J., "In-situ characterization of tungsten microcracking in selective laser melting," *Procedia CIRP*, vol. 74, 2018, pp. 107–110.

[16] Iveković, A., Omidvari, N., Vrancken, B., Lietaert, K., Thijs, L., Vanmeensel, K., Vleugels, J., and Kruth, J.-P., "Selective laser melting of tungsten and tungsten alloys," *International Journal of Refractory Metals and Hard Materials*, vol. 72, Dec. 2017, pp. 27–32.

[17] Gludovatz, B., Wurster, S., Weingärtner, T., Hoffmann, A., and Pippan, R., "Influence of impurities on the fracture behaviour of Tungsten," *Philosophical Magazine*, vol. 91, Jan. 2011, pp. 3006–3020.

[18] Woolf, P., "14.1: Design of experiments via Taguchi methods - orthogonal arrays," *Engineering LibreTexts* Available: https://eng.libretexts.org/Bookshelves/Industrial_and_Systems_Engineering/Book%3A_Chemical_Process_Dynamics_and_Controls_(Woolf)/14%3A_Design_of_Experiments/14.01%3A_Design_of_Experiments_via_Taguchi_Methods_-_Orthogonal_Arrays.

[19] "Production and characterization of hydrogen-reduced submicron tungsten powders," *Refractory Metals & Hard Materials*, vol. 10, Oct. 1991, pp. 133–141.

[20] Vesel, A., Mozetič, M., and Balat-Pichelin, M., "Sequential oxidation and reduction of tungsten/tungsten oxide," *Thin Solid Films*, vol. 591, Feb. 2015, pp. 174–181.

[21] Rupp, D., and Weygand, S. M., "Anisotropic fracture behaviour and brittle-to-ductile transition of polycrystalline tungsten," *Philosophical Magazine*, vol. 90, 2010, pp. 4055–4069.

[22] Box, J. F., *R.A. Fisher: The life of a scientist*, New York, NY: John Wiley & Sons, 1978.

[23] Fisher, R. A., *The Design of Experiments*, Oxford: 1935.

[24] *Standard test methods for tension testing of metallic materials*, West Conshohocken, PA: ASTM International, 2021.

[25] Kemnitz, R. A.; Sexton, B. M., RoomTemp.m, September 2021

[26] Kemnitz, R. A.; Sexton, B. M., 600C.m, September 2021

[27] *Standard test methods for hardness testing of metallic materials*, West Conshohocken, PA: ASTM International, 2021.

[28] Stat-Ease, "Design-Expert 13: Software for Design of Experiments.", 2021

[29] Anderson, T. L., *Fracture Mechanics: Fundamentals and Applications*, Boca Raton, FL: Taylor & Francis, 2005.

[30] Daniel, I. M., and Ishai, O., *Engineering mechanics of Composite Materials*, Delhi, India: Oxford University Press, 2007.

[31] Wang, D., Wu, S., Fu, F., Mai, S., Yang, Y., Liu, Y., and Song, C., "Mechanisms and characteristics of spatter generation in SLM processing and its effect on the properties," *Materials & Design*, vol. 117, 2017, pp. 121–130.

[32] Vincenti, W. G., and Kruger, C. H., *Introduction to Physical Gas Dynamics*, Malabar, FL: Krieger Publishing Company, 2002.

[33] Anderson, J. D., *Hypersonic and high-temperature gas dynamics*, Reston, VA: American Institute of Aeronautics and Astronautics, 2006.

[34] Liu, R., Wang, Z., Sparks, T., Liou, F., and Newkirk, J., "Aerospace applications of laser additive manufacturing," *Laser Additive Manufacturing*, 2017, pp. 351–371.

[35] Ren, C., Fang, Z. Z., Koopman, M., Butler, B., Paramore, J., and Middlemas, S., "Methods for improving ductility of Tungsten - A Review," *International Journal of Refractory Metals and Hard Materials*, vol. 75, 2018, pp. 170–183.

[36] Kemnitz, R. A. *W next steps working paper,* 14 February 2022

[37] Tekna, W-25 Spherical Tungsten Metal Powder, 2022.

REPORT DOCUMENTATION PAGE	*Form Approved OMB No. 074-0188*

The public reporting burden for this collection of information is estimated to average 1 hour per response, including the time for reviewing instructions, searching existing data sources, gathering and maintaining the data needed, and completing and reviewing the collection of information. Send comments regarding this burden estimate or any other aspect of the collection of information, including suggestions for reducing this burden to Department of Defense, Washington Headquarters Services, Directorate for Information Operations and Reports (0704-0188), 1215 Jefferson Davis Highway, Suite 1204, Arlington, VA 22202-4302. Respondents should be aware that notwithstanding any other provision of law, no person shall be subject to an penalty for failing to comply with a collection of information if it does not display a currently valid OMB control number.
PLEASE DO NOT RETURN YOUR FORM TO THE ABOVE ADDRESS.

1. REPORT DATE *(DD-MM-YYYY)*	2. REPORT TYPE	3. DATES COVERED *(From – To)*
24-03-2022	Master's Thesis	March 2021 – March 2022

TITLE AND SUBTITLE
Effects of a Nitrogen and Hydrogen Build Atmosphere on the Properties of Additively Manufactured Tungsten

5a. CONTRACT NUMBER

5b. GRANT NUMBER

5c. PROGRAM ELEMENT NUMBER

6. AUTHOR(S)

Madsen, Dana C., Captain, USAF

5d. PROJECT NUMBER

5e. TASK NUMBER

5f. WORK UNIT NUMBER

7. PERFORMING ORGANIZATION NAMES(S) AND ADDRESS(S)
Air Force Institute of Technology
Graduate School of Engineering and Management (AFIT/EN)
2950 Hobson Way, Building 640
WPAFB OH 45433-7765

8. PERFORMING ORGANIZATION REPORT NUMBER
AFIT-ENY-MS-22-M-306

9. SPONSORING/MONITORING AGENCY NAME(S) AND ADDRESS(ES)
Air Force Research Laboratory

10. SPONSOR/MONITOR'S ACRONYM(S)
AFRL/RXMS

11. SPONSOR/MONITOR'S REPORT NUMBER(S)

12. DISTRIBUTION/AVAILABILITY STATEMENT
DISTRUBTION STATEMENT A. APPROVED FOR PUBLIC RELEASE; DISTRIBUTION UNLIMITED.

13. SUPPLEMENTARY NOTES
This material is declared a work of the U.S. Government and is not subject to copyright protection in the United States.

14. ABSTRACT
Additively manufactured tungsten was printed in pure nitrogen, nitrogen-2.5% hydrogen, and nitrogen-5% hydrogen atmospheres as part of a 2^3 full factorial designed experiment and subjected to room-temperature and high-temperature three-point-bend testing, chemical analysis, hardness testing, and microstructural imaging techniques. The pure nitrogen specimens exhibited the highest strength and ductility at both high temperature and room temperature. Chemical analysis showed a 2-8x reduction in compositional oxygen relative to unprocessed powder. Hardness values for all samples was between 306.8 and 361.5 HV1. It is proposed that adding hydrogen into the build atmosphere reduced the available energy density for tungsten melting by introducing another competing reaction to that of nitrogen and oxygen, resulting in large cracks and pores in the material. These interruptions in the microstructure resulted in weaker, more brittle metal than that built in a pure nitrogen environment, but the results from the nitrogen environment were comparable in strength range to hot-rolled tungsten.

15. SUBJECT TERMS
Additive Manufacturing, Selective Laser Melting, Laser Powder Bed Fusion, Tungsten, Hydrogen, Nitrogen

16. SECURITY CLASSIFICATION OF:			17. LIMITATION OF ABSTRACT	18. NUMBER OF PAGES	19a. NAME OF RESPONSIBLE PERSON
a. REPORT	b. ABSTRACT	c. THIS PAGE			Ryan Kemnitz, AFIT/ENY
U	U	U	UU	109	19b. TELEPHONE NUMBER *(Include area code)* (937) 255-3636, ext 4775; ryan.kemnitz@afit.edu

Standard Form 298 (Rev. 8-98)
Prescribed by ANSI Std. Z39-18